DNA origami vaccines program antigen-focused germinal centers

Authors: Anna Romanov[1,2], Grant A. Knappe[1,3]*, Larance Ronsard[4]*, Heikyung Suh[2,5], Marjan Omer[1], Asheley P. Chapman[1, 5], Vanessa R. Lewis[2], Katie Spivakovsky[1], Josue Canales[6], Boris Reizis[6], Ryan D. Tingle[5,9], Christopher A. Cottrell[5,9], Torben Schiffner[5,9], Daniel Lingwood[4], Mark Bathe[1, 7, 8 †], Darrell J. Irvine[1, 2, 4, 5, 9, 10 †]

Affiliations:

[1]Department of Biological Engineering, Massachusetts Institute of Technology, Cambridge, MA 02139, United States

[2]Koch Institute for Integrative Cancer Research, Massachusetts Institute of Technology, Cambridge, MA 02139, United States

[3]Department of Chemical Engineering, Massachusetts Institute of Technology, Cambridge, MA 02139, United States

[4]Ragon Institute of Massachusetts General Hospital, Massachusetts Institute of Technology and Harvard University, Cambridge, MA 02139, United States

[5]Department of Immunology and Microbiology, The Scripps Research Institute, La Jolla, CA, 92037, United States

[6]Department of Pathology, New York University Grossman School of Medicine, New York, NY, United States

[7]Broad Institute of MIT and Harvard, Cambridge, MA 02139 United States

[8]Harvard Medical School Initiative for RNA Medicine, Harvard Medical School, Boston, MA, 02115, United States

[9]Consortium for HIV/AIDS Vaccine Development (CHAVD), The Scripps Research Institute, La Jolla, CA, 92037, United States

[10]Howard Hughes Medical Institute, Chevy Chase, MD, 20815, USA

(*These authors contributed equally to this work.)

([†] Co-corresponding authors. Email: djirvine@scripps.edu, mark.bathe@mit.edu)

Abstract

Recruitment and expansion of rare precursor B cells in germinal centers (GCs) is a central goal of vaccination to generate broadly neutralizing antibodies (bnAbs) against challenging pathogens such as HIV. Multivalent immunogen display is a well-established method to enhance vaccine-induced B cell responses, typically accomplished by using natural or engineered protein scaffolds. However, these scaffolds themselves are targets of antibody responses, with the potential to generate competitor scaffold-specific B cells that could theoretically limit expansion and maturation of “on-target” B cells in the GC response. Here, we rationally designed T-independent, DNA-origami based virus-like particles (VLPs) with optimal antigenic display of the germline

36 targeting HIV Env immunogen, eOD-GT8, and appropriate T cell help to achieve a potent GC
37 response. In preclinical mouse models, these DNA-VLPs expanded significantly higher
38 frequencies of epitope-specific GC B cells compared with a state-of-the-art clinical protein
39 nanoparticle. Optimized DNA-VLPs primed germinal centers focused on the target antigen and
40 rapidly expanded subdominant broadly neutralizing antibody precursor B cells for HIV with a
41 single immunization. Thus, avoiding scaffold-specific responses augments priming of bnAb
42 precursor B cells, and DNA-VLPs are a promising platform for promoting B cell responses towards
43 challenging subdominant epitopes.

44 **Main**

45 Generation of broadly neutralizing antibodies (bnAbs) that recognize diverse viral variants is a
46 central goal for successful vaccination against HIV[1] and universal vaccines for other pathogens
47 such as influenza[2, 3], coronaviruses[4], and dengue virus[5]. Precursor B cells capable of evolving to
48 produce bnAbs are characteristically rare in the naive repertoire and often have low affinity for
49 target immunogens[6]. Engaging rare B cell clones that belong to immunologically subdominant
50 bnAb lineages to promote their somatic hypermutation and affinity maturation in germinal centers
51 (GCs) remains an outstanding challenge and the primary aim of rational vaccine design[1, 7-10].

52 One powerful approach to augment humoral responses to vaccine antigens is via multivalent
53 display of many copies of an antigen on the surface of protein nanoparticles[11-19]. Nanoparticulate
54 antigens exhibit improved lymph trafficking[18, 20, 21] and enhance B cell receptor (BCR)
55 crosslinking[22, 23], inducing signal amplification downstream of the BCR[24] and enabling potent
56 valency-dependent B cell activation across a broad range of BCR affinities[25]. However,
57 multimerization of antigens on protein scaffolds may be a double-edged sword. When protein
58 scaffolds are used to display target antigens, they act as thymus-dependent (TD) repetitively
59 arrayed antigens themselves, eliciting priming of scaffold-specific B cells towards irrelevant
60 protein substrates that potentially compete in GCs against the desired, epitope-specific bnAb
61 precursor B cells[17, 26-30].

62 Scaffold-specific antibody responses against bacterially-derived scaffolds such as ferritin[17, 27, 28]
63 and lumazine synthase[29, 30], and computationally-designed two-component nanoparticles[26] have
64 been quantified via serology and neutralization assays in animal models and humans. However,
65 it remains poorly understood how these scaffold-specific competitor B cells shape the clonal
66 competition dynamics within GCs, which rely on finite populations of B cells and helper T cells.
67 While strategies to limit scaffold-specific responses have been used, such as glycosylation[30-32] or
68 physical masking of exposed scaffold epitopes[26, 33], they have generally failed to fully eliminate
69 off-target responses.

70 Importantly, the presence of competitive scaffold-specific B cells could lead to several outcomes
71 that remain unclear due to the lack of suitable tools to test these hypotheses: 1) these B cells may
72 outcompete antigen-specific GC B cells for limited T cell help and antigen availability[9], particularly
73 if the scaffold is more immunogenic than the antigen itself[34]; 2) they might contribute to
74 immunological imprinting or 'original antigenic sin' upon repeated dosing or repurposing of the
75 nanoparticle platform[35, 36], and 3) they could lead to high titers of anti-scaffold antibodies that
76 facilitate epitope masking and antibody feedback that alters the subsequent immune response[37].

Each of these competitive effects are of particular concern when designing a vaccine against immunologically subdominant epitopes, such as the CD4 binding site (CD4bs) in HIV Env antigens, which is the target of VRC01-class bnAbs[26]. This task is further complicated by the extremely low frequency of bnAb precursor B cells in the naive B cell repertoire[6, 34, 38].

One strategy to prime these rare subdominant precursors is immunization with engineered germline targeting immunogens, such as the engineered outer domain of gp120, eOD-GT8, which was designed to bind germline reverted VRC01-class BCRs with high affinity[39]. A protein nanoparticle form of eOD-GT8 (eOD-GT8 60mer) was developed by fusing eOD-GT8 with the self-assembling bacterial protein lumazine synthase (LumSyn); 60 copies of LumSyn self-assemble to form an icosahedral nanoparticle displaying eOD-GT8 at high density on the particle surface[38, 40]. This ~30 nm protein nanoparticle has been shown to effectively activate VRC01-class B cell precursors in humanized mouse models and is currently undergoing clinical trials as a germline targeting immunogen for VRC01-class bnAbs against HIV[29, 41, 42]. While eOD-GT8 60mer has been shown to successfully activate VRC01-class precursor B cells in humans[29], it also elicits a strong LumSyn-specific antibody response[29, 30], and it remains unknown whether, and how, this scaffold-specific response may limit the priming of the “on-target” bnAb precursors of interest. Because germline targeting immunizations are just the first step toward shepherding B cells to become bnAb producers, it is critical that precursor activation and expansion be as efficient as possible[1, 43].

As an alternative to protein-based scaffolds, we previously demonstrated that virus-like particles (VLPs) formed by the programmed assembly of thymus-independent (TI) DNA origami (DNA-VLPs) enable precise antigen display[44] and enhance antigen-specific antibody titers while avoiding anti-scaffold B cell responses, as there is no thymus-dependent (protein) substrate except for the antigen[28]. Furthermore, DNA origami has been shown to be minimally immune-stimulatory[45, 46], unless specific CpG motifs are included to activate innate Toll-like receptor pathways[47, 48]. Thus, DNA origami may serve as an attractive vaccine scaffold due to its highly programmable geometry and size[49, 50], quantitative spatial precision for display of biomolecular cargoes[51,52], and immunologically inert TI scaffold. Accordingly, we hypothesized that DNA origami scaffolds could enable a rigorous test of the effects of scaffold-specific competitor B cells on the recruitment and affinity maturation of rare “on-target” precursors in primary GCs.

To test our hypothesis, we rationally designed icosahedral DNA-VLPs conjugated with eOD-GT8 as a clinically-relevant test immunogen. We identified a set of DNA-VLP design rules, principally optimizing antigen density, particle size, and incorporating synthetic T cell helper epitopes to trigger follicular targeting of the VLPs, which led to 15-fold higher frequencies of antigen-specific GC B cells compared to eOD-GT8 monomer. In a humanized mouse model of VRC01-class B cell priming, we found that GCs formed by scaffold-silent DNA-VLPs contained 25-fold higher ratios of on-target epitope-specific B cells to competitor B cells — approximately 12 times higher than the protein-based eOD-GT8 60mer nanoparticles that elicited significant scaffold-specific competitor responses. Further, DNA-VLPs effectively expanded VRC01-class precursors within 14 days following low-dose immunization, conditions where the protein nanoparticle failed to expand bnAb-lineage B cells. Thus, eliminating competitive scaffold-specific humoral responses

118 can have a substantial impact on the priming of rare B cell precursors, with DNA-VLPs showing
119 promise as a platform technology to prime antigen-focused germinal center responses.

120 **Scaffolding eOD-GT8 on DNA origami virus-like particles**

121 We previously demonstrated that SARS-CoV-2 receptor-binding domain multimerized on
122 icosahedral DNA-VLPs (30 antigens/nanoparticle) elicited high serum IgG titers in mice after a
123 prime-boost vaccination that potently neutralized the virus[28]. To begin exploring how DNA-VLP
124 design impacts earlier stages of the immune response, and particularly the formation of primary
125 germinal center responses that are crucial to effective HIV vaccines, we employed the same DNA-
126 VLP and surface-conjugated 30 equally spaced copies of the eOD-GT8 antigen to the particles
127 (Fig. 1a). This wireframe DNA origami nanoparticle was computationally designed using
128 DAEDALUS software[49, 53] and synthesized following established protocols, utilizing a custom
129 ssDNA scaffold folded with 30 DBCO-modified staple oligonucleotides and reacted with eOD-GT8
130 containing a C-terminal azido linker[51, 52] (Supplementary Fig. 1). Successful DNA-VLP self-
131 assembly was confirmed through agarose gel electrophoresis (AGE) and dynamic light scattering
132 (Extended Data Fig. 1a-c). Post-antigen coupling, the hydrodynamic radius of the nanoparticles
133 was ~40 nm, which we annotate as d40_30mer. The percentage of alkyne groups on the DNA-
134 VLP successfully conjugated with antigen was quantified using a bicinchoninic acid protein assay;
135 functionalization efficiency across independent sample preparations was consistently in the range
136 of 90-100%. The measured antigen concentrations were used to standardize eOD-GT8 doses
137 across experimental groups (Extended Data Fig. 1d). Cryo-electron microscopy and negative
138 stain transmission electron microscopy validated the preservation of the icosahedral geometry of
139 the origami structure post-antigen conjugation (Fig. 1b, Extended Data Fig. 1e). The bioavailability
140 and proper orientation of the antigen were further confirmed through binding assays with murine
141 VRC01, a broadly neutralizing antibody targeting the CD4 binding site of gp120 that binds with
142 high affinity to eOD-GT8[39]. VRC01 antibody successfully bound eOD-GT8 displayed on DNA-
143 VLPs, as evidenced by decreased mobility in gel electrophoresis (Supplementary Fig. 2a). As a
144 functional quality control metric for antigen bioactivity, we incubated antigen-loaded particles with
145 Ramos B cells expressing the germline VRC01 B cell receptor, and measured calcium flux using
146 a calcium-dependent fluorescent dye. Consistent with previous findings[44], culture of VRC01-
147 expressing Ramos B cells with 5 nM eOD-GT8-functionalized DNA-VLPs led to rapid B cell
148 activation as assessed by calcium signaling, while the same dose of soluble eOD-GT8 monomer
149 failed to trigger calcium release (Fig. 1c).

150 **d40_30mer DNA-VLPs enhance serum antibody titers in prime-boost immunization but are**
151 **weak priming immunogens**

152 Based on the results from *in vitro* B cell activation and previous *in vivo* studies of eOD-GT8 protein
153 nanoparticles[25], we hypothesized that d40_30mer would induce higher antibody responses in
154 mice compared to eOD-GT8 monomer due to its multivalency. For immunization studies, we
155 employed a saponin-MPLA nanoparticle adjuvant (SMNP), a potent ISCOMs-like adjuvant[54]. We
156 verified that mixing DNA-VLPs with SMNP did not affect the stability of the DNA-VLPs
157 (Supplementary Fig. 2b). C57BL/6 mice were primed and boosted with equimolar doses of eOD-
158 GT8 monomer or d40_30mer co-administered with SMNP, and antigen-specific serum IgG titers
159 were monitored over time. Both eOD-GT8 monomer control and DNA-VLPs resulted in weak

160 responses post-prime, but following boosting the DNA-VLP elicited endpoint antibody titers ~1 log
161 higher than the eOD-GT8 monomer (Fig. 1d). We additionally assessed antibody responses
162 against the bare DNA-VLP, and consistent with our prior studies[28], we observed no elevation in
163 anti-origami IgG or anti-dsDNA IgG after prime or boost (Fig. 1e, Extended Data Fig. 2a,b). We
164 also measured IgM responses to dsDNA and detected no response above the nonspecific
165 background triggered by protein eOD-GT8/SMNP immunization in the complete absence of DNA
166 (Extended Data Fig. 2c).

167 To gain insight into the early stages of the response to monomer vs. DNA-VLP immunization, we
168 evaluated germinal center responses in draining lymph nodes at two weeks after a single
169 immunization by flow cytometry (Supplementary Fig. 3). Unexpectedly, immunization with
170 d40_30mer did not increase the number of GC B cells ($B220^{+}/CD38^{lo}$ $GL7^{hi}$) or follicular helper T
171 cells ($CD4^{+}/CXCR5^{hi}$ $PD1^{hi}$) relative to eOD-GT8 monomer vaccination (Fig. 1f-g). The frequency
172 and counts of antigen-specific GC B cells, which were identified by fluorescent eOD-tetramer
173 staining, were also not enriched and remained low— below 1% (Fig. 1h). Alternative adjuvants
174 including alum, AddaVax, AS01b, and CpG ODN 1826 also did not enhance GC B cell responses
175 elicited by the DNA-VLPs (Extended Data Fig. 3).

176 A primary concern for DNA origami-based nanoparticles *in vivo* is whether they remain stable over
177 a sufficient time period in the presence of DNAses present in tissues. To test whether the priming
178 efficiency of DNA-VLPs was limited by endonuclease-mediated degradation, we assessed
179 vaccine responses in DNase I-deficient mice (Extended Data Fig. 4a)[55, 56]. We verified via serum
180 stability assays that d40_30mer remained intact in DNase I KO serum for longer than seven days
181 (Extended Data Fig. 4b). Further, we validated that mutant DNase I KO mice established robust
182 GCs in response to protein nanoparticle vaccination identically to WT controls (Extended Data
183 Fig. 4c). To determine if DNAse-mediated particle degradation was a limiting factor *in vivo*, we
184 primed WT or DNase I KO mice with d40_30mer and analyzed germinal centers after two weeks.
185 Surprisingly, total GC size, Tfh responses, and antigen-specific GC B cells formed by d40_30mer
186 in DNase I KO animals were low and identical to responses in WT littermates (Extended Data Fig.
187 4d). These data suggested that the d40_30mer nanoparticle design may provide sufficient avidity
188 to expand antibody-producing cells upon boosting, but the nanoparticle design, irrespective of
189 enzymatic stability, is not optimal for supporting primary GC responses.

190 **d40_30mer DNA-VLPs have restricted access to follicular dendritic cells**

191 To understand why the d40_30mer DNA-VLP poorly primed GC responses, we considered the
192 physiological barriers limiting antigen delivery to B cells *in vivo*. Antigen arriving at draining lymph
193 nodes during primary immunization is often quickly cleared by lymph flow, protease activity in the
194 tissue, or by endocytosis and degradation by lymphocytes[20, 57-59]. Alternatively, antibody- or
195 complement-opsonized antigen can be captured by follicular dendritic cells (FDCs) and presented
196 to B cells in germinal centers for prolonged periods to support the GC response[60-63]. We thus
197 analyzed antigen biodistribution in draining lymph nodes (dLNs) following immunization,
198 comparing eOD-GT8 monomer and d40_30mer DNA-VLPs with the protein nanoparticle eOD-
199 GT8 60mer (hereafter, p60mer), which we have previously shown becomes decorated with
200 complement *in vivo* via the lectin pathway, leading to rapid robust accumulation on FDCs (which

express high levels of complement receptor)[61]. To better understand the *in vivo* fate of DNA-VLPs versus protein immunogens, we immunized mice with fluorescently tagged antigens and collected inguinal dLNs two hours later for cryo-sectioning and immunofluorescence staining. Early after immunization, eOD-GT8 monomer was primarily detected in central non-follicular areas of dLNs, largely colocalizing with F4/80$^+$ medullary sinus macrophages (MSMs) (Fig. 2a, b). By contrast, eOD-GT8 delivered as d40_30mer was present at substantially higher levels in the draining lymph nodes, and colocalized with CD169$^+$ subcapsular sinus macrophages (SSMs) lining the edges of the lymph node and MSMs (Fig. 2a, b). The p60mer particle also colocalized with SSMs but was already at this early timepoint accumulating on the dendrites of CD35$^+$ FDCs (Fig. 2a lower panel, white arrows). Quantitative pixel analysis revealed that d40_30mer and p60mer had similar levels of antigen colocalization with SSMs (Fig. 2c), but only p60mer showed enrichment on FDCs (Fig. 2c). At later time points such as day 7, p60mer had become highly concentrated on FDCs, whereas follicles in lymph nodes immunized with d40_30mer had no retention of fluorescent antigen (Fig. 2d). Thus, antigen trafficking and retention of DNA-VLPs was distinct from similarly-sized protein nanoparticles.

We hypothesized that trapping of d40_30mer in the subcapsular sinus could be due to high expression of DNA-binding scavenger receptors on macrophages and/or lymphatic endothelial cells[64] or inadequate triggering of complement pathways to mediate the capture of the particles by FDCs[62]. To test the first hypothesis, we passivated d40_30mer by coating it with polylysine-PEG polymer[65], which has been used *in vivo* with other DNA origami formulations for stabilization, charge neutralization[66, 67], and avoidance of macrophage uptake[68, 69]. PEGylated d40_30mer exhibited enhanced stability in mouse serum and reduced association with murine macrophage cells *in vitro* (Extended Data Fig. 5a-c). However, d40_30mer nanoparticles with or without PEGylation showed similar patterns of early accumulation in medullary and subcapsular sinus regions (Supplementary Fig. 5d), and PEG-coated DNA-VLPs elicited weaker germinal centers compared to the uncoated d40_30mer (Extended Data Fig. 5e-h), likely due to interference of the polylysine-PEG coating with antigen recognition on BCRs[70].

Heavily glycosylated nanoparticle-antigens become decorated with complement *in vivo* via the lectin pathway, when mannose binding lectin (MBL, an innate immune protein present in blood and lymph) binds to the particles and triggers complement deposition[61, 71]. To test the hypothesis of insufficient complement activation by the DNA-VLPs, we measured binding of MBL and C3 from naïve mouse serum to eOD-GT8 monomer, d40_30mer, or p60mer particles immobilized on ELISA plates. MBL and C3 both showed significantly lower binding to eOD-GT8 monomer and d40_30mer compared to p60mer (Fig. 2e, f). Similarly, very little binding of recombinant MBL to eOD-GT8 monomer or d40_30mer was detected by ELISA compared to p60mer (Extended data Fig. 6). Thus, DNA-VLPs exhibited considerably less effective engagement of the lectin pathway for complement activation than the p60mer nanoparticles.

Engineering DNA-VLPs with high antigen density induces follicle targeting and augments antigen-specific GC B cell responses

We hypothesized that poor complement activation explained the lack of FDC accumulation of the DNA-VLPs, and that this was a result of insufficient antigen density on the DNA origami scaffold[71]. MBL is a large protein complex consisting of trimeric stalks containing a collagen domain and

243 carbohydrate-binding domain (CBD), which oligomerize forming hexamers. Each CBD in the stalk
244 trimer is estimated to be ~5 nm apart from its neighbor with similar or larger distances to CBDs in
245 neighboring stalks of the oligomer[72]. Each CBD has weak, millimolar affinity for mannose, but
246 strong binding can be achieved through the avidity of multiple CBD stalks binding to numerous
247 glycans[61]; thus MBL binding is highly sensitive to the density of glycans on a viral or bacterial
248 surface. To assess the role of antigen density on MBL binding and complement activation by DNA-
249 VLPs, we synthesized a set of 4 different particles, with diameters of approximately ~23 or ~34
250 nm, functionalized with either 30 or 60 copies of eOD-GT8 (Fig. 3a), providing a range of predicted
251 glycan densities (0.04 to 0.14 glycans/nm^2) and a range of inter-antigen distances from 11 nm
252 (the original d40_30mer) down to 4.5-6 nm between neighboring antigens (d30_60mer, Fig. 3b).
253 Upon antigen conjugation, which was quantified by BCA (Extended Data Fig. 1d), the
254 hydrodynamic diameter of these particles was measured by DLS to be approximately ~30 nm and
255 ~40 nm, respectively, denoted as d30 and d40 (Extended Data Fig. 1c). Each of the 4 DNA-VLP
256 designs had sufficient avidity to robustly activate cognate B cells and elicited indistinguishable
257 calcium flux in germline VRC01-Ramos B cells *in vitro* (Fig. 3c). Amongst these designs, antigen
258 attachment sites in d30_60mer are spaced similarly to the distances between CBD domains on
259 MBL, and this design also closely resembles the geometric configuration of eOD-GT8 antigen on
260 lumazine synthase p60mer.

261 We conducted complement deposition assays with fresh mouse serum to evaluate how antigen
262 spacing affected MBL and C3 deposition on the DNA-VLP surfaces, using the p60mer
263 nanoparticle as a positive control for the assay. We observed a monotonic increase in both MBL
264 and C3 deposition on DNA-VLPs as antigen density increased, with the highest amount of
265 complement depositing on d30_60mer (Fig. 3d, e, Extended data Fig. 6b). MBL binding with
266 d30_60mer was nearly identical to p60mer; however, the amount of C3 opsonized on DNA-VLPs
267 was significantly lower. Next, we immunized mice with the panel of DNA-VLPs and harvested
268 dLNs for cleared lymph node imaging at day 4 after injection. Strikingly, fluorescent eOD-GT8
269 signal was detected in lymph nodes from all groups, but colocalization with FDCs was only
270 observed for d30_60mer particles (Fig. 3f). Thus, as previously observed with other synthetically
271 mannosylated protein nanoparticles[71], stronger deposition of MBL on DNA-VLPs, which can be
272 increased by increasing antigen density, correlates with increased antigen capture on FDCs *in*
273 *vivo*.

274 Next, we investigated how antigen density impacts germinal center formation. Mice immunized
275 with equimolar antigen doses of eOD-GT8 monomer or DNA-VLPs showed similar total counts of
276 GC B cells and Tfh cells two weeks post immunization (Fig. 3g, h). However, we observed a ~15-
277 fold increase in the frequency and 10-fold increase in total counts of eOD-specific GC B cells
278 elicited by the d30_60mer compared to the eOD-GT8 monomer control (Fig. 3i). Thus, a DNA-
279 VLP design that promoted particle capture by FDCs correlated with substantially stronger
280 expansion of antigen-specific B cells in active GCs. Furthermore, this effect was driven by antigen
281 density, rather than valency, since the d40_60mer failed to elicit antigen capture on FDCs or
282 expansion of antigen-specific cells.

283

284 **Synthetic T cell epitopes provide focused T cell help to antigen-specific GC B cells**

285 In addition to retention of antigen on FDCs, stimulation of GC B cells by helper CD4 T cells is a
286 critical cue for driving strong germinal center reactions[9, 73]. DNA-VLPs are T-independent
287 scaffolds; therefore, all T cell epitopes must be derived from the conjugated protein antigen. In
288 contrast, protein scaffolds such as lumazine synthase that forms the basis of the p60mer provide
289 abundant scaffold-derived T cell help[74]. Consequently, following p60mer immunization, antigen-
290 specific B cells compete with scaffold-specific B cells for co-stimulation from the same pool of
291 CD4 T cells recognizing scaffold-derived peptides. Given the small size of the eOD-GT8 antigen,
292 which may provide insufficient T cell help on its own, we next tested whether the incorporation of
293 the universal helper peptide pan-HLA DR-binding epitope (PADRE) on the terminus of the antigen
294 could further amplify GC responses elicited by DNA-VLPs without introducing off-target B cell
295 epitopes. PADRE binds with high affinity to a broad spectrum of human and mouse MHC
296 haplotypes and has been shown to be safe in human clinical trials[75-77]. We tested this hypothesis
297 by comparing GC responses induced by three different 60mer formulations: d30_60mer,
298 d30_60mer carrying eOD-PADRE (d30_60mer-PADRE), and p60mer. Fusion of the T cell epitope
299 to eOD-GT8 had no effect on formation of the DNA-VLPs (polydispersity, diameter, or antigen
300 functionalization efficiency**,** Extended Fig. 1f). Furthermore, all three 60mers strongly activated
301 germline VRC01 Ramos B cells *in vitro* (Fig. 4a) and bound MBL and C3 in mouse serum
302 (Extended Data Fig. 6c).

303 We primed mice with the three 60mer formulations and assessed serum IgG titers by ELISA and
304 GC responses by flow cytometry**.** The addition of PADRE significantly enhanced early anti-eOD-
305 GT8 IgG responses compared to d30_60mer (Fig. 4b), while minimal IgG responses were
306 detected against the PADRE epitope itself (Fig. 4c). Mice primed with d30_60mer-PADRE also
307 had significantly increased frequencies and total counts of GC B cells and Tfh cells compared to
308 d30_60mer, though the total GC B cell count remained 4-fold lower than that elicited by LumSyn-
309 scaffolded p60mer (Fig. 4d, e). However, GCs initiated by d30_60mer-PADRE expanded a much
310 higher frequency of eOD-specific GC B cells (30-40%) compared to p60mer (~5%, Fig. 4f). This
311 was also reflected in the total counts of eOD-specific GC B cells, which were highest in d30-
312 60mer-PADRE immunizations (2.1-fold greater than p60mer), despite the induction of an overall
313 smaller GC response than that produced by p60mer. Thus, engineering of T cell help in DNA-
314 VLPs enabled priming of a robust antigen-focused GC response.

315 **DNA-VLPs prime epitope-focused germinal centers in humanized mice**

316 We hypothesized that the increased frequency of antigen-specific B cells in germinal centers
317 activated by DNA-scaffolded compared to protein-scaffolded antigen may reflect an "immune
318 focusing" effect of DNA-VLP immunization due to the inert nature of the DNA origami scaffold[28].
319 To directly assess competitor versus "on-target" epitope-specific B cell responses directed to the
320 CD4 binding site (CD4bs), we analyzed germinal center responses to protein- or DNA-scaffolded
321 immunogens in transgenic mice expressing the germline human IGHV1-2*02 gene segment
322 knocked into the mouse Ig locus (V_H1-2 mice), which is paired with endogenous mouse light
323 chains. This mouse model is designed to assess the engagement of engineered germline
324 targeting immunogens with a diverse repertoire of VRC01-class B cell precursors expressing
325 human heavy chains, modeling the diversity of potential bnAb precursor B cells present in the
326 human B cell repertoire, with a low frequency of bona fide bnAb precursors[78]. We immunized V_H1-

327 2 mice with d30_60mer-PADRE or p60mer and analyzed their GC responses in draining lymph
328 nodes, using flow probes to characterize antigen-specific vs. competitor B cells in GCs (Fig. 5a).

329 To assess on-target responses, we analyzed the staining of $IgM^{-}IgD^{-}$ GC B cells by fluorescently
330 labeled eOD-60mer nanoparticle probes and an eOD-60mer-CD4bsKO nanoparticle probe, the
331 latter of which contain mutations in the CD4 binding site that ablate binding by true VRC01-class
332 precursor B cells; binding to this KO probe identifies B cells specific to eOD epitopes other than
333 the CD4bs. Importantly, it has been previously observed that antibodies previously identified by
334 intact eOD-60mer nanoparticle probes do not bind lumazine-specific B cells[30]. This suggests that
335 scaffold-specific responses primed by p60mer represent B cells which recognize breakdown
336 products of the protein nanoparticle that we have previously shown are rapidly generated by
337 extrafollicular proteases in the lymph node [59]. For quantifying scaffold-specific competitor B cells,
338 we used fluorescently labeled bare lumazine synthase or bare DNA-VLPs to stain GC B cells.
339 Comparing GC B cell binding to these different sets of nanoparticle probes quantifies relative
340 frequencies of "on-target" CD4bs-specific ($eOD^{++}KO^{-}$) and "off-target" (CD4bs-KO^{+} or scaffold-
341 specific) clones in GCs.

342

343 As observed in WT mice, the p60mer primed overall slightly larger total GC responses (2-fold
344 greater than the DNA-VLP, Fig. 5b). However, we observed that the composition of GCs elicited
345 by protein- and DNA-scaffolded antigen was very distinct: GCs formed in mice immunized with
346 d30_60mer-PADRE were composed of nearly ~60% on-target CD4bs-specific GC B cells
347 (identified by $eOD^{++}KO^{-}$ gate), compared to ~20% expanded by p60mer (Fig. 5c). Furthermore,
348 the on-target B cells expanded by the DNA-VLP formulation had stronger staining by the antigen
349 probes represented by higher mean fluorescence intensity, suggesting that these cells might have
350 undergone higher extents of affinity maturation (Fig. 5d). Following p60mer immunization,
351 LumSyn-specific B cells contributed to ~13% of the GC, comparable in magnitude to the on-target
352 CD4bs-directed response (Fig. 5d). When staining with bare DNA-VLP probes, some background
353 staining was detected in GC B cells, but this staining was the same in mice primed with either
354 DNA-VLPs and p60mer, and similar low levels of background binding were detected on B cells
355 from naïve mice (Fig. 5f, Supplementary Fig. 7), which may reflect low-level scavenger receptor
356 expression in B cells[79]. Compared to the p60mer, DNA-VLP immunization promoted germinal
357 centers that contained 25-fold higher ratios of on-target CD4bs-specific B cells to off-target
358 competitors (Fig. 5g), whereas in p60mer the frequency of epitope-specific B cells was only
359 enriched 2-fold.

360 **eOD display by DNA-VLPs leads to more efficient priming of bnAb precursors and robust**
361 **somatic hypermutation**

362 Finally, we inquired whether the epitope-focused GCs produced by DNA-VLPs led to better
363 expansion and somatic hypermutation (SHM) of VRC01-class precursors, which are defined by
364 IGHV1-2*02 usage combined with 5-amino acid CDRL3 light chains. The V_H1-2 mouse model has
365 a diversity of V(D)J-rearranged human V_H1-2 heavy chains and a fully murine LC repertoire,
366 where only about 0.15% of B cells express 5-AA light chains in the naïve repertoire[78], thus
367 providing a stringent model for expanding VRC01-class precursors. We immunized V_H1-2 mice

368 with 5 µg (eOD-GT8 equivalent) of either d30_60mer-PADRE or p60mer, sorted class-switched
369 antigen-specific GC B cells ($B220^{+}/CD38^{lo}GL7^{hi}/IgM^{-}IgG^{+}/eOD^{++}KO^{-}$) on day 14, and performed
370 single-cell sequencing to analyze the BCR repertoire. A total of 444 and 465 BCR sequences
371 were recovered and analyzed for d30_60mer-PADRE and p60mer, respectively.

372 We found diverse BCR clonotypes (defined as shared CDRH3 usage) expanded by each
373 immunogen (Fig. 6a, c). However, in DNA-VLP vaccination, several clonotypes contained
374 significantly more expanded representatives (Fig. 6a), suggesting proliferation of clonally related
375 B cell lineages in the GCs, aligning with our hypothesis of epitope-focused GCs. We further note
376 that within these clonotypes, DNA-VLP immunization enriched for the five AA CDRL3 VRC01
377 class signature (Fig. 6b), whereas the p60mer did not (Fig. 6d). The p60mer was previously
378 reported to enrich for this signature V_H1-2 mice after a single prime immunization but this required
379 antigen doses of 30 ug or more and 2-8 weeks[78]. Importantly, within the clonotypes expanded by
380 DNA-VLP vaccination, the five amino acid CDRL3 signature was enriched by expansion of public
381 B cell clones (BCRs with shared CDRH3 + CDRL3 within the independent vaccine recipients;
382 Clone IDs - 70, 78, 116, 62, 19 and 137) (Fig. 6a, right, Extended Data Fig. 7). Expansion of
383 multiple genetically identical B cell clones in different mice points to a reproducible mechanism
384 for triggering of VRC01 bnAb class precursors with DNA-VLPs. The 5 AA CDRL3 was supplied
385 by usage of mouse IGKV4-61*01 (Extended Data Fig. 7), as described in a previous study[40]. We
386 also observed SHM in the vaccine-expanded B cells primed with both formulations, but they were
387 not significantly different at this early timepoint. We also identified enrichment of key VRC01-class
388 HC mutations[80] in both formulations, particularly S55R/N mutations (Extended Data Fig. 8). Thus,
389 epitope-focused GCs primed by DNA-VLPs can augment the maturation of bnAb precursors.

390 **Discussion**

391 Anti-scaffold B cell responses have been previously reported for almost all protein-based
392 nanoparticle scaffolds[17, 26, 28-30, 81, 82], and their effects on limiting on-target immune responses and,
393 consequently, the development of a successful vaccine against pathogens such as HIV, are still
394 incompletely understood. Thus far, anti-scaffold antibodies have been thought to be minimally
395 concerning for immunodominant antigens[26], or potentially even beneficial by improving antigen
396 capture in lymph nodes or masking scaffold epitopes in future boosts[17]. However, for subdominant
397 antigens like HIV Env, anti-scaffold responses have been shown to dominate the serum antibody
398 response[26], and it has not yet been investigated how these competitor B cells influence primary
399 GC dynamics. While strategies such as glycosylation[30-32], PEGylation[26, 33], and PASylation[26] have
400 been introduced to reduce scaffold-specific responses, such approaches are known to be
401 imperfect. Further, even with perfect masking of exposed scaffold epitopes on assembled
402 nanoparticles, degradation of these nanoparticles by tissue proteases that are abundant in lymph
403 node sinuses[59] may expose new epitopes that contribute to competitor scaffold-specific
404 responses. Thus, our understanding of the role of protein scaffold competition on humoral immune
405 responses remains incomplete due to limited tools and materials to test these effects of altering
406 scaffolds without changing properties like geometry or antigen display.

407 Here, we instead used T-independent, inert DNA origami vaccine scaffolds to assess the impact
408 of distracting epitopes on the potency of germinal center responses towards a displayed antigen,
409 eOD-GT8. Notably, we found that high valency of 60 antigens and high antigen and glycan density

410 of DNA-VLPs was critical for engaging complement pathways and promoting follicle retention and
411 expanding antigen-specific B cells in GCs, whereas larger particles or particles with lower antigen
412 copy numbers failed. Intriguingly, the optimal d30_60mer nanoparticle design closely mimicked
413 the geometry of the clinical p60mer nanoparticle[29, 38], and both particles were effectively
414 recognized by MBL from mouse serum. However, the amount of C3 on DNA-VLPs was
415 significantly lower compared to the protein nanoparticle, which may arise due to the porosity,
416 surface charge, and interaction of DNA-VLPs with complement binding proteins, which may
417 potentially limit downstream complement activation[83, 84]. This remains a design element that can
418 be further improved for the DNA origami platform. Second, we found that augmenting the small
419 eOD-GT8 immunogen with synthetic T cell epitopes substantially improved the immunogenicity
420 of DNA-VLPs. Lumazine synthase and other protein scaffolds have been shown to have intrinsic
421 T cell epitopes[74]; here we found that by adding a synthetic T cell epitope (PADRE) to the DNA-
422 VLP, we could recapitulate scaffold-derived T cell help without introducing off-target epitopes for
423 B cells.

424 Since our optimized DNA-VLP 60mer was similar to the clinical p60mer nanoparticles in regard
425 to antigen valency, spacing, nanoparticle geometry, and presence of T cell help, we were also
426 able to assess the effect of the scaffold material on the subsequent clonal competition in GC
427 responses. GCs expanded by DNA-VLPs were significantly more epitope-specific than those
428 induced by the LumSyn-based protein nanoparticle. We attribute this focusing effect due to the
429 undiluted T cell help provided to the eOD-specific B cells, whereas in p60mer vaccination, antigen-
430 and scaffold-specific B cells compete for LumSyn-derived Tfh help. We characterized the ratio of
431 on-target CD4bs-specific B cells to off-target competitors (scaffold-specific B cells or non-CD4bs
432 specific B cells) in the V_H1-2 rearranging mouse model[78] by staining lymphocytes with antigen
433 and scaffold-only flow cytometry probes. GCs primed by DNA-VLPs were significantly more
434 focused on the displayed antigen compared to GCs generated by p60mer, where lumazine-
435 specific B cells competed in the GC at high frequency. Our BCR sequencing analysis confirms
436 that epitope-focusing of the GCs enhances the priming of bnAb precursors, as evidenced by the
437 increased number of VRC01-class precursors expanded by immune focused GCs primed with
438 DNA-VLPs compared to the more competitive GCs primed by p60mer. Furthermore, DNA-VLPs
439 reproducibly primed these VRC01 precursors across multiple animals. In future work, DNA-VLPs
440 may be evaluated side by side with protein nanoparticles in heterologous boosting regimes to
441 understand the effect of scaffold responses upon re-exposure, where feedback and imprinting
442 mediated by pre-existing scaffold antibodies and T cell memory may be more apparent[85].

443 Collectively, our results emphasize the importance of nanoscale antigen organization on lymph
444 node delivery and illustrate that T-dependent versus -indepedent scaffold material may
445 significantly influence clonal competition dynamics in GCs and their ability to prime desirable
446 subdominant B cell clones, with currently unknown yet important potential consequences on
447 limiting successful vaccine design for challenging pathogens such as HIV.

448 We demonstrate that DNA-VLPs are a promising, modular T-independent scaffold that is highly
449 programmable and capable of producing potent and directed B cell responses using a clinical
450 germline targeting immunogen, but several important issues related to potential clinical translation
451 of are of interest for future work, such as evaluating DNA-VLP degradation due by extracellular

452 nucleases. Additionally, while in our work we did not detect any class-switched anti-DNA or -VLP
453 antibody responses, autoimmune risks posed by antibody responses to DNA/protein hybrids must
454 be carefully evaluated.

455 **References**

456

457 1. Haynes, B.F. et al. Strategies for HIV-1 vaccines that induce broadly neutralizing
458 antibodies. *Nature Reviews Immunology* **23**, 142-158 (2023).
459 2. Guthmiller, J.J. et al. Broadly neutralizing antibodies target a haemagglutinin anchor
460 epitope. *Nature* **602**, 314-320 (2022).
461 3. Paules, C.I., Marston, H.D., Eisinger, R.W., Baltimore, D. & Fauci, A.S. The Pathway to a
462 Universal Influenza Vaccine. *Immunity* **47**, 599-603 (2017).
463 4. Chen, Y. et al. Broadly neutralizing antibodies to SARS-CoV-2 and other human
464 coronaviruses. *Nature Reviews Immunology* **23**, 189-199 (2023).
465 5. Durham, N.D. et al. Broadly neutralizing human antibodies against dengue virus
466 identified by single B cell transcriptomics. *eLife* **8**, e52384 (2019).
467 6. Abbott, R.K. et al. Precursor Frequency and Affinity Determine B Cell Competitive
468 Fitness in Germinal Centers, Tested with Germline-Targeting HIV Vaccine Immunogens.
469 *Immunity* **48**, 133-146.e136 (2018).
470 7. Ng'uni, T., Chasara, C. & Ndhlovu, Z.M. Major Scientific Hurdles in HIV Vaccine
471 Development: Historical Perspective and Future Directions. *Front. Immunol.* **11**, 590780
472 (2020).
473 8. McGuire, A.T. et al. Engineering HIV envelope protein to activate germline B cell
474 receptors of broadly neutralizing anti-CD4 binding site antibodies. *Journal of*
475 *Experimental Medicine* **210**, 655-663 (2013).
476 9. Victora, G.D. & Nussenzweig, M.C. Germinal Centers. *Annu. Rev. Immunol.* **40**, 413-442
477 (2022).
478 10. Steichen, J.M. et al. A generalized HIV vaccine design strategy for priming of broadly
479 neutralizing antibody responses. *Science* **366** (2019).
480 11. Schiller, J.T., Castellsagué, X. & Garland, S.M. A Review of Clinical Trials of Human
481 Papillomavirus Prophylactic Vaccines. *Vaccine* **30**, F123-F138 (2012).
482 12. Mohsen, M.O. & Bachmann, M.F. Virus-like particle vaccinology, from bench to bedside.
483 *Cellular & Molecular Immunology* **19**, 993-1011 (2022).
484 13. Cohen, A.A. et al. Mosaic nanoparticles elicit cross-reactive immune responses to
485 zoonotic coronaviruses in mice. *Science* **371**, 735-741 (2021).
486 14. Brune, K.D. et al. Plug-and-Display: decoration of Virus-Like Particles via isopeptide
487 bonds for modular immunization. *Sci Rep* (2016).
488 15. Ols, S. et al. Multivalent antigen display on nanoparticle immunogens increases B cell
489 clonotype diversity and neutralization breadth to pneumoviruses. *Immunity* **56**, 2425-
490 2441.e2414 (2023).
491 16. Song, J.Y. et al. Safety and immunogenicity of a SARS-CoV-2 recombinant protein
492 nanoparticle vaccine (GBP510) adjuvanted with AS03: A randomised, placebo-
493 controlled, observer-blinded phase 1/2 trial. *eClinicalMedicine* **51** (2022).
494 17. Kanekiyo, M. et al. Self-assembling influenza nanoparticle vaccines elicit broadly
495 neutralizing H1N1 antibodies. *Nature* **499**, 102-106 (2013).
496 18. Singh, A. Eliciting B cell immunity against infectious diseases using nanovaccines.
497 *Nature Nanotechnology* **16**, 16-24 (2021).
498 19. Marcandalli, J. et al. Induction of Potent Neutralizing Antibody Responses by a Designed
499 Protein Nanoparticle Vaccine for Respiratory Syncytial Virus. *Cell* **176** (2019).

20. Bachmann, M.F. & Jennings, G.T. Vaccine delivery: a matter of size, geometry, kinetics and molecular patterns. *Nat. Rev. Immunol.* **10**, 787-796 (2010).
21. Irvine, D.J. & Read, B.J. Shaping humoral immunity to vaccines through antigen-displaying nanoparticles. *Current Opinion in Immunology* **65**, 1-6 (2020).
22. Batista, F.D. & Neuberger, M.S. B cells extract and present immobilized antigen: implications for affinity discrimination. *The EMBO Joural* **19**, 513-520 (2000).
23. Batista, F.D. & Harwood, N.E. The who, how and where of antigen presentation to B cells. *Nature Reviews Immunology* **9**, 15-27 (2009).
24. Brooks, J.F. et al. Molecular basis for potent B cell responses to antigen displayed on particles of viral size. *Nature Immunology* **24**, 1762-1777 (2023).
25. Kato, Y. et al. Multifaceted Effects of Antigen Valency on B Cell Response Composition and Differentiation In Vivo. *Immunity* **53**, 548-563.e548 (2020).
26. Kraft, J.C. et al. Antigen- and scaffold-specific antibody responses to protein nanoparticle immunogens. *Cell Reports Medicine* **3**, 100780 (2022).
27. Sliepen, K. et al. Interplay of diverse adjuvants and nanoparticle presentation of native-like HIV-1 envelope trimers. *npj Vaccines* **6**, 103 (2021).
28. Wamhoff, E.-C. et al. Enhancing antibody responses by multivalent antigen display on thymus-independent DNA origami scaffolds. *Nature Communications* **15**, 795 (2024).
29. Leggat, D.J. et al. Vaccination induces HIV broadly neutralizing antibody precursors in humans. *Science* **378**, eadd6502 (2022).
30. Schiffner, T. et al. Diverse competitor B cell responses to a germline-targeting priming immunogen in human Ig loci transgenic mice. *bioRxiv*, 2024.2001.2022.575410 (2024).
31. Duan, H. et al. Glycan Masking Focuses Immune Responses to the HIV-1 CD4-Binding Site and Enhances Elicitation of VRC01-Class Precursor Antibodies. *Immunity* **49**, 301-311 (2018).
32. Martina, C.E., Crowe, J.E., Jr. & Meiler, J. Glycan masking in vaccine design: Targets, immunogens and applications. *Front. Immunol.* **14** (2023).
33. Eto, Y. et al. Optimized PEGylated Adenovirus Vector Reduces the Anti-vector Humoral Immune Response against Adenovirus and Induces a Therapeutic Effect against Metastatic Lung Cancer. *Biological and Pharmaceutical Bulletin* **33**, 1540-1544 (2010).
34. Abbott, R.A.-O. & Crotty, S.A.-O. Factors in B cell competition and immunodominance. *Immunological Reviews* **296**, 120-131 (2020).
35. Wheatley, A.K. et al. Immune imprinting and SARS-CoV-2 vaccine design. *Trends Immunol* **42** (2021).
36. Schiepers, A. et al. Molecular fate-mapping of serum antibody responses to repeat immunization. *Nature* **615**, 482-489 (2023).
37. Zarnitsyna, V.I., Lavine, J., Ellebedy, A., Ahmed, R. & Antia, R. Multi-epitope Models Explain How Pre-existing Antibodies Affect the Generation of Broadly Protective Responses to Influenza. *PLOS Pathogens* **12**, e1005692 (2016).
38. Jardine, J.G. et al. HIV-1 broadly neutralizing antibody precursor B cells revealed by germline-targeting immunogen. *Science* **351**, 1458-1463 (2016).
39. Jardine, J. et al. Rational HIV immunogen design to target specific germline B cell receptors. *Science* **340**, 711-716 (2013).
40. Jardine, J.G. et al. Priming a broadly neutralizing antibody response to HIV-1 using a germline-targeting immunogen. *Science* **349**, 156-161 (2015).
41. deCamp, A.C. et al. Human immunoglobulin gene allelic variation impacts germline-targeting vaccine priming. *medRxiv*, 2023.2003.2010.23287126 (2023).
42. Cohen, K.W. et al. A first-in-human germline-targeting HIV nanoparticle vaccine induced broad and publicly targeted helper T cell responses. *Science Translational Medicine* **15**, eadf3309 (2023).

43. Andrabi, R., Bhiman, J.N. & Burton, D.R. Strategies for a multi-stage neutralizing antibody-based HIV vaccine. *Curr. Opin. Immunol.* **53** (2018).
44. Veneziano, R. et al. Role of nanoscale antigen organization on B-cell activation probed using DNA origami. *Nat. Nanotechnol.* **15**, 716-723 (2020).
45. Wamhoff, E.-C. et al. Evaluation of Nonmodified Wireframe DNA Origami for Acute Toxicity and Biodistribution in Mice. *ACS Applied Bio Materials* **6**, 1960-1969 (2023).
46. Lucas, C.R. et al. DNA Origami Nanostructures Elicit Dose-Dependent Immunogenicity and Are Nontoxic up to High Doses In Vivo. *Small* (2022).
47. Du, R.R. et al. Innate Immune Stimulation Using 3D Wireframe DNA Origami. *ACS Nano* (2022).
48. Comberlato, A., Koga, M.M., Nüssing, S., Parish, I.A. & Bastings, M.M.C. Spatially Controlled Activation of Toll-like Receptor 9 with DNA-Based Nanomaterials. *Nano Letters* **22**, 2506-2513 (2022).
49. Jun, H. et al. Rapid prototyping of arbitrary 2D and 3D wireframe DNA origami. *Nucleic Acids Res.* **49**, 10265-10274 (2021).
50. Rothemund, P.W.K. Folding DNA to create nanoscale shapes and patterns. *Nature* **440**, 297-302 (2006).
51. Knappe, G.A., Wamhoff, E.-C. & Bathe, M. Functionalizing DNA origami to investigate and interact with biological systems. *Nature Reviews Materials* **8**, 123-138 (2023).
52. Knappe, G.A., Wamhoff, E.-C., Read, B.J., Irvine, D.J. & Bathe, M. In Situ Covalent Functionalization of DNA Origami Virus-like Particles. *ACS Nano* **15**, 14316-14322 (2021).
53. Veneziano, R. et al. Designer nanoscale DNA assemblies programmed from the top down. *Science* **352**, 1534 (2016).
54. Silva, M. et al. A particulate saponin/TLR agonist vaccine adjuvant alters lymph flow and modulates adaptive immunity. *Science Immunology* **6**, eabf1152 (2021).
55. Bradley, A. et al. The mammalian gene function resource: the International Knockout Mouse Consortium. *Mamm Genome* (2012).
56. Lacey, K.A. et al. Secreted mammalian DNases protect against systemic bacterial infection by digesting biofilms. *Journal of Experimental Medicine* **220**, e20221086 (2023).
57. Cyster, J.G. B cell follicles and antigen encounters of the third kind. *Nature Immunology* **11**, 989-996 (2010).
58. Swartz, M.A., Hubbell, J.A. & Reddy, S.T. Lymphatic drainage function and its immunological implications: From dendritic cell homing to vaccine design. *Seminars in Immunology* **20**, 147-156 (2008).
59. Aung, A. et al. Low protease activity in B cell follicles promotes retention of intact antigens after immunization. *Science* **379**, eabn8934 (2023).
60. Gonzalez, S.F. et al. Complement-Dependent Transport of Antigen into B Cell Follicles. *The Journal of Immunology* **185**, 2659-2664 (2010).
61. Tokatlian, T. et al. Innate immune recognition of glycans targets HIV nanoparticle immunogens to germinal centers. *Science* **363**, 649-654 (2019).
62. Phan, T.G., Grigorova, I., Okada, T. & Cyster, J.G. Subcapsular encounter and complement-dependent transport of immune complexes by lymph node B cells. *Nature Immunology* **8**, 992-1000 (2007).
63. Reddy, S.T. et al. Exploiting lymphatic transport and complement activation in nanoparticle vaccines. *Nature Biotechnology* **25**, 1159-1164 (2007).
64. Taban, Q., Mumtaz, P.T., Masoodi, K.Z., Haq, E. & Ahmad, S.M. Scavenger receptors in host defense: from functional aspects to mode of action. *Cell Communication and Signaling* **20**, 2 (2022).

600 65. Ponnuswamy, N. et al. Oligolysine-based coating protects DNA nanostructures from low-
601 salt denaturation and nuclease degradation. *Nat. Commun.* **8**, 15654 (2017).
602 66. Zeng, Y.C. et al. Fine tuning of CpG spatial distribution with DNA origami for improved
603 cancer vaccination. *Nature Nanotechnology* (2024).
604 67. Wang, W.X. et al. Universal, label-free, single-molecule visualization of DNA origami
605 nanodevices across biological samples using origamiFISH. *Nature Nanotechnology* **19**,
606 58-69 (2024).
607 68. Rodríguez-Franco, H.J., Weiden, J. & Bastings, M.M.C. Stabilizing Polymer Coatings
608 Alter the Protein Corona of DNA Origami and Can Be Engineered to Bias the Cellular
609 Uptake. *ACS Polymers Au* **3**, 344-353 (2023).
610 69. Koga, M.M., Comberlato, A., Rodríguez-Franco, H.J. & Bastings, M.M.C. Strategic
611 Insights into Engineering Parameters Affecting Cell Type-Specific Uptake of DNA-Based
612 Nanomaterials. *Biomacromolecules* **23**, 2586-2594 (2022).
613 70. Wamhoff, E.-C. et al. Controlling Nuclease Degradation of Wireframe DNA Origami with
614 Minor Groove Binders. *ACS Nano* **16**, 8954-8966 (2022).
615 71. Read, B.J. et al. Mannose-binding lectin and complement mediate follicular localization
616 and enhanced immunogenicity of diverse protein nanoparticle immunogens. *Cell*
617 *Reports* **38**, 110217 (2022).
618 72. Sheriff, S., Chang Cy Fau - Ezekowitz, R.A. & Ezekowitz, R.A. Human mannose-binding
619 protein carbohydrate recognition domain trimerizes through a triple alpha-helical coiled-
620 coil. *Nature Stuctural Biology* (1994).
621 73. Ramiscal, R.R. & Vinuesa, C.G. T-cell subsets in the germinal center. *Immunological*
622 *Reviews* **252** (2013).
623 74. Xu, Z. et al. Incorporation of a Novel CD4+ Helper Epitope Identified from Aquifex
624 aeolicus Enhances Humoral Responses Induced by DNA and Protein Vaccinations.
625 *iScience* **23**, 101399 (2020).
626 75. La Rosa, C. et al. Clinical Evaluation of Safety and Immunogenicity of PADRE-
627 Cytomegalovirus (CMV) and Tetanus-CMV Fusion Peptide Vaccines With or Without
628 PF03512676 Adjuvant. *The Journal of Infectious Diseases* **205**, 1294-1304 (2012).
629 76. Alexander, J. et al. Development of high potency universal DR-restricted helper epitopes
630 by modification of high affinity DR-blocking peptides. *Immunity* **1**, 751-761 (1994).
631 77. Alexander, J. et al. Linear PADRE T Helper Epitope and Carbohydrate B Cell Epitope
632 Conjugates Induce Specific High Titer IgG Antibody Responses1. *The Journal of*
633 *Immunology* **164**, 1625-1633 (2000).
634 78. Tian, M. et al. Induction of HIV Neutralizing Antibody Lineages in Mice with Diverse
635 Precursor Repertoires. *Cell* **166**, 1471-1484.e1418 (2016).
636 79. Domange Jordö, E., Wermeling, F., Chen, Y. & Karlsson, M.C.I. Scavenger receptors as
637 regulators of natural antibody responses and B cell activation in autoimmunity. *Molecular*
638 *Immunology* **48**, 1307-1318 (2011).
639 80. Caniels, T.G. et al. Germline-targeting HIV-1 Env vaccination induces VRC01-class
640 antibodies with rare insertions. *Cell Reports Medicine* **4** (2023).
641 81. Heinimäki, S. et al. Antigenicity and immunogenicity of HA2 and M2e influenza virus
642 antigens conjugated to norovirus-like, VP1 capsid-based particles by the
643 SpyTag/SpyCatcher technology. *Virology* **566**, 89-97 (2022).
644 82. Brinkkemper, M. et al. Mosaic and mixed HIV-1 glycoprotein nanoparticles elicit antibody
645 responses to broadly neutralizing epitopes. *PLOS Pathogens* **20**, e1012558 (2024).
646 83. Moghimi, S.M. et al. Material properties in complement activation. *Advanced Drug*
647 *Delivery Reviews* **63**, 1000-1007 (2011).
648 84. Trouw, L.A., Nilsson Sc Fau - Gonçalves, I., Gonçalves I Fau - Landberg, G., Landberg
649 G Fau - Blom, A.M. & Blom, A.M. C4b-binding protein binds to necrotic cells and DNA,

limiting DNA release and inhibiting complement activation. *J Exp Med* **12**, 1937-1948 (2005).
85. Schiepers, A., Van't Wout, M.F.L., Hobbs, A., Mesin, L. & Victora, G.D. Opposing effects of pre-existing antibody and memory T cell help on the dynamics of recall germinal centers. *Immunity* **57**, 1618-1628 (2024).

Methods

Ethics Statement

All animal studies were performed under an institutional animal care and use committee-approved animal protocol (MIT CAC protocol # 2303000488**)** following local, state, and National Institutes of Health guidelines for the care and use of animals. This research does not include human participants.

Mice

Six-to-ten-week-old female C57BL/6 mice were purchased from The Jackson Laboratory (strain no. 000664). V_H1-2 mice (gift courtesy of Dr. Frederick Alt) were bred in-house and genotyped using Transnetyx. DNase I KO mice were provided by the Reizis lab at NYU Langone (original source CMMR MGI:103157) and rederived for subsequent experiments. For DNase I KO experiments, heterozygous mice were bred, pups were genotyped using PCR (Supplementary Table 2), and wildtype littermates were used as controls.

ssDNA scaffold synthesis

Custom-length DNA scaffolds for DNA-VLPs were synthesized as previously described[86]. Briefly, SS320 *E. coli* cells were co-transformed with the corresponding plasmid and the M13cp helper plasmid (originally provided by Andrew Bradbury, Los Alamos National Laboratories). Pre-cultures of the transformed cells were grown overnight at 37 °C in 2x YT medium containing 100 µg/ml ampicillin and 15 µg/ml chloramphenicol). Cells were pelleted by centrifuging three times at 4000 g for 3 min and subsequently discarded. Phage was precipitated from the supernatant in presence of 6% (w/v) PEG_{8kDa} and 3% (w/v) of NaCl by stirring at 4 °C for 1 h and harvested by centrifugation at 20,000 g at 4 °C for 1 h. After resuspension in TE buffer, ssDNA was extracted via the EndoFree GigaPrep purification protocol with the following modifications: Proteinase K was added to buffer P1 followed by incubation at 37 °C for 1 h, addition of buffer P2 and incubation at 70 °C for 10 min. After ssDNA purification, Triton X-144 was used to remove residual endotoxins to levels less than 0.2 EU/µmol DNA scaffold, corresponding to less than 0.000015 EU/injection into mice. Endotoxin levels were measured using ToxinSensor Gel Clot Endotoxin Assay Kits. Purity of the scaffolds was analyzed by agarose gel electrophoresis (AGE)(1.6% agarose, TAE buffer with 12 mM $MgCl_2$, EtBr, 60 V for 150 min at room temperature).

Oligonucleotide synthesis

DBCO-modified oligonucleotides were fabricated in-house. A (#10-1000), C (#10-1010), G (#10-1020), T (#10-1030), and DBCO-TEG (#10-1941) phosphoramidites and ancillary synthesis reagents were acquired from Glen Research and used following the manufacturer's recommendations. Phosphoramidites were dissolved and diluted in anhydrous acetonitrile to 0.1

690 M prior to synthesis. Oligonucleotides were synthesized on a Biolytic Dr. Oligo 192c
691 oligonucleotide synthesizer, at a 200 nmol scale with CPG 1000 Å standard base supports (#20-
692 2001, #20-2011, #20-2021, #20-2031 from Glen Research) in normal mode under nitrogen.
693 Synthesis success and yield was observed by monitoring the penultimate trityl-cleavage.
694 Following the synthesis, oligonucleotides were cleaved and deprotected under pressure at 55°C
695 for 2 hr in 30% ammonium hydroxide (Thermo Fisher Scientific, cat# 423305000,). The cleaved
696 strands were desalted with acetonitrile and eluted in nuclease-free water. The DBCO-modified
697 oligonucleotides were purified by Glen-Pak™ DNA 30 mg in a 96-Well Plate (#60-5400-01) under
698 reduced pressure following the manufacturer's protocols. After purification, the oligonucleotides
699 were dried and resuspended in 1x TE and stored at 4°C. Oligonucleotide concentrations and
700 yields were determined via UV-Vis measurements (Tecan Spark). Oligonucleotide purity was
701 confirmed by HPLC (Waters Acquity System).

702 **Immunogen synthesis**

703 eOD-GT8 monomer (with C-terminal 6x-His and cysteine), eOD-PADRE monomer (with N-
704 terminal 6x-His and cysteine and C-terminal PADRE), and eOD-60mer were synthesized as
705 previously reported[40]. Briefly, plasmids were transiently transfected into Expi293F cells. After 5
706 days of culturing in conditions described above, cell culture supernatants were collected and
707 protein was purified in an AKTA pure chromatography system using HiTrap HP Ni sepharose
708 affinity column, followed by size exclusion chromatography using Superdex 75 Increase 10/300
709 GL column (GE Healthcare). Endotoxin levels in purified protein were measured using Endosafe
710 Nexgen-PTS system (Charles River) and were ensured to be less than 5EU/mg protein. The eOD-
711 60mer was affinity purified by incubating with *Galanthus nivalis* lectin-conjugated agarose beads
712 (Vector Laboratories, AL-1243-5,) overnight under gentle agitation at 4°C and eluted with lectin
713 elution buffer containing 1 M methyl a-D-mannopyranoside (Millipore Sigma, M6882,). The
714 resulting solution was dialyzed in PBS and further purified by size-exclusion chromatography
715 using Superdex 200 Increase 10/300GL. Bare lumazine synthase was produced by BlueSky
716 Bioservices as previously described[29]. Briefly, lumazine synthase from Aquifex aeolicus was
717 expressed in E.Coli, cells were lysed, supernatant was heat-treated for 30 min at 75°C and
718 supernatant was again clarified by centrifugation. Fully assembled particles were purified by two
719 successive size-exclusion chromatographies, using Superdex 75 and Sephacryl 500 columns,
720 respectively.

721 To add a terminal azide for SPAAC reactions, eOD-Cys monomers were reduced with 5 molar
722 excess of TCEP, then desalted into PBS + 10 mM EDTA using Zeba 7K MWCO desalting columns
723 (Thermo Fisher, cat# 89883). The number of free cysteines was confirmed using an Ellman's
724 assay. The azide linker was formed by reacting 60 mM SMCC (Thermo Fisher Scientific, cat
725 #A35394) with 1.1x excess of Azido-PEG3-Amine (Broadpharm, cat#BP-20580) for 1 hour at
726 room temperature. Reduced antigen was reacted with 5 molar excess of azide linker for 4 hours
727 at room temperature, and unreacted linker was then removed by spin filter centrifugation in
728 Amicon 10K MWCO centrifugal filters (Millipore Sigma, cat# UFC801008). Antigen was
729 concentrated to approximately 300 μM for SPAAC reactions.

730 **DNA-VLP synthesis and characterization**

731 DNA-VLPs were assembled as previously described[53]. All designs were generated using
732 DAEDALUS[53] (d40 VLP) or ATHENA[49] (d30 VLP) with staples manually adjusted in Tiamat
733 software[87] to have outward nick positions (2 per edge). To fold origami, 30 nM of scaffold was
734 mixed with 5–10x excess of each oligonucleotide staple in TAE buffer with 12 mM $MgCl_2$ and
735 thermally annealed as follows: 95°C for 5 min, 80–75°C at 1°C per 5 min, 75–30°C at 1°C per 15
736 min, and 30–25°C at 1°C per 10 min. DNA-VLPs were purified into PBS using Amicon Ultra 100
737 kDa centrifugal filters (Millipore Sigma, cat #UFC810024) spun at 2000g and stored at 4 °C. Purity
738 and dispersity of DNA-VLPs were validated by AGE (1.6% agarose, TAE buffer with 12 mM $MgCl_2$,
739 SYBR Safe, 65V for 150 min) and dynamic light scattering. For antigen conjugation, DNA-VLPs
740 were concentrated to >1 μM and reacted with at least 3 molar equivalents of eOD-Azide for 24
741 hours at 37°C. Excess antigen was removed by drop dialysis into 1X PBS for 16 hours (Millipore
742 Sigma, mixed cellulose ester, 0.025 μm) and the purified nanoparticles were diluted to 100 nM
743 and stored at 4°C. Antigen functionalization was validated using AGE (1.6% agarose, TAE buffer
744 with 12 mM $MgCl_2$, SYBR Safe, 65V for 150 min) and quantified using bicinchoninic acid
745 colorimetric assay.

746 **Negative stain transmission electron microscopy**

747 Uranyl formate staining was performed as previously described[28]. Briefly, DNA-VLPs were diluted
748 to 3–5 nM in PBS and 5 μL was applied onto glow-discharged electron microscopy grids. After 30
749 seconds, the grids were blotted with filter paper and washed with 5 μL of fresh 2% uranyl formate
750 solution containing 5 mM NaOH for 30 seconds. The uranyl formate solution was removed by
751 blotting on filter paper, and the grids were stored with a desiccant before imaging. TEM was
752 performed on an FEI Tecnai G2 Spirit Twin. Shown are images at 30K, 42K, or 67K magnifications.

753 **CryoEM imaging**

754 Three microliters of the folded and purified DNA-VLP solution (approximately 300 nM) was applied
755 onto the glow-discharged 200-mesh Quantifoil 2/1 grid, blotted for four seconds and rapidly frozen
756 in liquid ethane using a Vitrobot Mark IV (Thermo Fisher Scientific). Grids were screened and
757 imaged on a Talos Arctica cryo-electron microscope (Thermo Fisher Scientific) operated at 200
758 kV at a magnification of 79,000× (corresponding to a calibrated sampling of 1.76 Å per pixel).
759 Micrographs were recorded by EPU software (Thermo Fisher Scientific) with a Gatan K2 Summit
760 direct electron detector in counting mode, where each image is composed of 24 individual frames
761 with an exposure time of 6 s and a total dose ~63 electrons per Å2. We used a defocus range of
762 –1.0 – –2.5 μm to collect images, which were subsequently motion-corrected using MotionCor2.
763 Particle picking was performed manually using Relion[88] with a particle box size of 320.

764 **In vitro B cell activation assays**

765 Calcium flux assays were conducted as previously described[44]. Ramos B cells expressing
766 germline VRC01 BCRs were stained with 10 μM Fluo-4 AM (Thermo Fisher Scientific, cat#
767 F14217) for 30 min at 37 °C. After washing twice in serum-free RPMI medium, calcium flux assays
768 were performed in triplicate on a Tecan plate reader at 37 °C on a 96-well microplate with 160 μl
769 of Fluo-4 labelled Ramos cells at 2 million cells per ml. A baseline fluorescence was then recorded
770 for 1 min, and 40 μl of antigens were added to the cells for a final concentration of 5 nM of antigen.
771 Raw calcium traces were normalized to a common baseline by subtracting the PBS time trace at

every time point, then dividing the time trace at every point by the average of the time points before antigen addition.

Dye labeling of nanoparticles for imaging and flow probes

Protein antigens (eOD-GT8 monomers, eOD-60mer, and lumazine synthase) at 1 mg/mL were desalted into PBS and diluted 1:1 with 0.2M sodium bicarbonate buffer. Dye stocks (AF488-NHS-ester, AF647-NHS ester, AF555-NHS ester) (Thermo Fisher Scientific, cat# A20000, A20006, A20009) were prepared in DMSO, and added at 5-molar excess and reacted with antigens at 1 hour at room temperature. Due to lower efficiency of labeling lumazine synthase, reactions were performed overnight with shaking (500 rpm). Excess dye was removed by passing proteins through Zeba Spin Desalting Columns (Thermo Fisher Scientific). DNA-VLPs (d30) used as flow probes were formulated with 6 DBCO-modified oligos and reacted with 10 molar excess of AF488-Azide or AF555-Azide triethylammonium salt (Thermo Fisher Scientific, cat# A10266, A20012). Excess dye was removed by drop dialysis into 1X PBS for 16 hours (Millipore Sigma, mixed cellulose ester, 0.025 µm). For flow staining, eOD-tetramers were produced by first biotinylating Avi-tagged eOD-GT8 monomers (without PADRE) with BirA (Avidity, Inc), and mixing an excess of biotinylated eOD-GT8 monomer with fluorescently labeled Streptavidin-PE, Streptavidin-AF647, or Streptavidin-BV421 (BioLegend cat# 405203, 405237, 405226) step-wise on ice.

Immunizations

SMNP adjuvant was prepared as previously described[54]. Antigen formulations were prepared by diluting 5 µg of the indicated antigens mixed with 5 µg of SMNP adjuvant per mouse in 1X PBS and gently mixed with a pipette. Mice (6-10 weeks old) were shaved at the tail base and immunized subcutaneously at the left and right sides of the tail base (50 µL per side). For adjuvant screening, the following formulations were used and prepared in 100 µL total volumes per mouse: SMNP (5 µg/mouse), alum in the form of Alhydrogel (InvivoGen, 100 µg/mouse), AddaVax (InvivoGen, 1:1 v/v), AS01b (GSK, 1:1 v/v), and ODN 1826 (IDT, 50 µg/mouse).

Flow cytometry analysis of GC B and Tfh cells

Mice were euthanized at the indicated time point post-injection by CO_2 asphyxiation, and inguinal lymph nodes were collected and mechanically digested into a single-cell suspension using Biomasher tubes and a motorized tissue grinder. Lymphocytes were strained twice through 60 µm Multi-Screen Mesh filter plates (Millipore Sigma, cat# MANMN6010) and washed once in 1X PBS. The cells were then stained with 1:750 dilution of Zombie UV Live Dead Stain (BioLegend, cat# 423107) diluted in PBS for 10 minutes at room temperature. Excess dye was removed by washing once with FACS buffer (1X PBS, 2% FBS, 0.01% sodium azide). The cells were then resuspended in 25 µL FACS buffer containing Fc block (BioLegend, cat# 156603) and incubated on ice for 15 minutes. Antibody mixes (2X stock) were prepared in FACS buffer and contained the following antibodies: anti-CD4 BUV737 (BD Biosciences, RM4.5), anti-B220 APC-Cy7 or PE-Cy7 (BioLegend, RA3-6B2), anti-CD38-AF488 or BV421 (BioLegend, 90), anti-GL7 PerCpCy5.5 (BioLegend, GL7), anti-CXCR5 BV605 (BioLegend, L138D7), anti-PD1-AF647 or BV421 (BioLegend, 29F.1A12), and antigen tetramer probes. For the experiment shown in Fig. 5, anti-IgM-PE-Cy7 (BioLegend, MA-69) and anti-IgD-BV785 (BioLegend, 11-26c.2a) were also included in the antibody cocktail. Tetramers were added to antibody mix so that the final amount per sample

813 was 50 ng. For nanoparticle probes (Fig 5 & 6), nanoparticle probes were added at 5 ng/ sample.
814 The cells in Fc block were mixed with antibody and probe mixture and incubated for 30 minutes
815 on ice, then washed twice with FACS buffer. The cells were fixed with 2% PFA, washed once and
816 stored in FACS buffer until flow cytometry analysis. The cells were transferred to U-bottom 96-
817 well plates and mixed with CountBright Absolute Counting beads (Thermo Fisher Scientific, cat#
818 C36950) before analysis. Flow cytometry was carried out on a BD LSR Fortessa or Symphony
819 A3 cytometer in plate-mode. Full-minus-one (FMO) staining controls were included in every
820 experiment for drawing gates.

821 **Lymph node microscopy**

822 For lymph node histology, mice were immunized with 5 µg of fluorescently labeled eOD-GT8
823 monomer, DNA-VLPs, or protein nanoparticles and sacrificed at the indicated time points. Mice
824 were euthanized by CO_2 asphyxiation, and inguinal lymph nodes were flash frozen in OCT
825 embedding medium and sectioned on a Leica Cryostat (10 µm thick sections) and stored at –
826 80°C. For immunostaining, the sections were quickly thawed, fixed with 10% neutral buffered
827 formalin, and blocked/permeabilized with PBS containing 2% BSA and 0.01% Triton-X. The
828 sections were then stained with 1:100 dilutions of anti-CD35-BV421 (BD Biosciences, clone
829 8c12), anti-CD169-AF488 (BioLegend clone 3D6.112), or anti-F4/80 (BioLegend clone BM8) in
830 block/perm buffer for 1 hour in a humidity chamber. The slides were washed three times in PBS
831 and mounted with ProLong Diamond Antifade mountant (Thermo Fisher Scientific) and secured
832 with sealant. Slides were stored in the dark and imaged on a Leica Sp8 Laser Scanning Confocal
833 Microscope with 25x water-based objective. Colocalization between channels was quantified
834 using a MATLAB script which applied a Gaussian filter to each channel, created a binary mask to
835 identify FDC or SSMs, and calculated the fraction of area occupied by antigen signal. In ImageJ,
836 LUT tables were selected to optimize contrast and enhance readability for color-blindness.

837 For cleared lymph node imaging, mice were immunized with 5 or 10 µg of fluorescently labeled
838 nanoparticles (specified in captions). For in situ follicle labeling, 4 µg of anti-CD35-BV421 (BD,
839 clone 8c12) was injected subcutaneously 12–16 hours prior to tissue harvesting. Inguinal lymph
840 nodes were isolated and fixed in 4% PFA for 24 hours and cleared using DISCO as previously
841 described[61]. Briefly, LNs were washed twice in PBS and excess fat and connective tissue were
842 removed. Nodes were then gradually moved into solutions containing successively higher
843 concentrations of methanol until they were incubated for half an hour in pure methanol. Nodes
844 were then bleached in hydrogen peroxide for one minute before being returned to methanol for
845 half an hour. They were then gradually transferred into solutions containing increasing
846 concentrations of tertiary-butanol before eventually being incubated in pure tertiary-butanol 0.4%
847 α-tocopherol for one hour. Nodes were then removed from solution and allowed to dry completely
848 before being placed in dichloromethane. After the lymph nodes dropped to the bottom of tubes
849 following swirling, they were stored in dibenzyl ether with 0.4% α-tocopherol. Follicles were
850 imaged using an Olympus FV1200 Laser Scanning Confocal Microscope at 10x magnification
851 over a 300 µm distance. Lasers were set to minimize pixel saturation in the brightest samples.
852 Images were analyzed using ImageJ software. LUT tables were selected to optimize contrast and
853 enhance interpretability for color-blindness.

854 **Passivation of DNA-VLPs with polylysine-PEG**

855 DNA-VLPs (d40_30mer) were coated with polylysine-PEG1K or 5K (Alamanda Polymers) at 1:1
856 N:P ratio, as previously described[65], and complexes were analyzed by AGE (1.6% agarose, TAE
857 buffer with 12 mM $MgCl_2$, SYBR Safe, 60V for 150 min at room temperature). For serum stability
858 analysis, d40_30mer was incubated with or without polymer coating at 37°C in the presence of
859 10% mouse serum (freshly isolated from C57BL/6 mice) and analyzed by AGE as described
860 previously. For macrophage association, RAW264.7 murine macrophages were seeded into 24-
861 well plates and incubated with 10 nM AF647-labeled d40_30mer with or without PEG coating.
862 After 2 hrs of incubation, the cells were thoroughly washed, and nanoparticle signal was analyzed
863 by flow cytometry. Lymph node imaging and measurement of GC responses induced by
864 vaccination with uncoated or coated DNA-VLPs were performed as described above.

865 **ELISA analysis of serum antibody responses**

866 Blood samples were collected from immunized mice via retro-orbital or submandibular bleeds and
867 serum was isolated using centrifugation through Serum Gel tubes (Sarstedt) and stored at –20°C.
868 MaxiSorp plates (Thermo Fisher Scientific) were coated with 2 µg/ml protein immunogens (eOD-
869 GT8 monomer, eOD-CD4bs-KO monomer, or Lumazine Synthase) overnight at 4°C. For anti-
870 dsDNA and anti-VLP ELISAs, ELISA plates were first coated first with 100 ug/mL poly-D-lysine in
871 1X PBS and incubated at 37°C for 1 hr. The plates were washed once with PBS and then
872 incubated with 10 µg/mL of bare DNA-VLPs (d30) or calf-thymus DNA (Sigma Aldrich) overnight
873 at 4°C. The plates were blocked with Casein block buffer (G-Biosciences). Plates were washed
874 four times in 1x PBS containing 0.2% Tween-20, and dilutions of serum in blocking buffer were
875 added and incubated for two hours. A commercial dsDNA antibody (Abcam, clone 35I9) was used
876 as a positive control in anti-DNA assays, and murine VRC01 was included in all anti-eOD-GT8
877 ELISAs. Plates were washed four times and an HRP-conjugated goat anti-mouse IgG (BioRad)
878 was added and incubated for one hour. Plates were then washed and TMB was added. The
879 reaction was stopped with sulfuric acid once the wells containing the lowest dilutions of TMB
880 began to develop visually and the absorbance of each well was determined. All titers reported are
881 inverse dilutions where A450nm – A540nm (reference wavelength) equals 0.2 or as area under
882 the curve measurements (specified in figure captions). Anti-DNA IgM ELISAs were performed
883 using a commercial assay (Alpha Diagnostic International, cat# 5130) following manufacturer
884 instructions.

885 **C3 and MBL ELISAs**

886 ELISA plates were first coated with 100 µg/mL poly-D-lysine in 1X PBS and incubated at 37°C for
887 1 hr. The plates were washed with DPBS, then coated with nanoparticles overnight at 4°C (DNA-
888 VLP concentrations were normalized so that final eOD concentration was 1 µg/mL). The plates
889 were blocked with 1X PBS containing calcium and magnesium with 1% BSA, then washed 4 times
890 with 1X PBS containing 0.2% Tween-20. Fresh mouse serum was collected from naive C57BL/6
891 mice in Sarstedt serum gel tubes and kept on ice. Serum was diluted in blocking buffer (starting
892 at 30% v/v) and further diluted in 1:2 dilution series. Serum dilutions were transferred to ELISA
893 plates and incubated for 1 hr at 37°C. For recombinant mouse MBL assays, MBL2 (Biotechne
894 R&D, cat #2208) was diluted in blocking buffer starting at 100 ug/mL concentration and diluted
895 1:2. The plates were washed 4 times as before, then incubated with 2 µg/mL rat anti-mouse MBL
896 antibody (Abcam, clone 14D12) or rat anti-mouse C3 antibody (Abcam, clone 11H9) diluted in

897 blocking buffer. The plates were washed four times, then incubated with 1:5000 HRP-conjugated
898 mouse-adsorbed goat anti-rat IgG (Bio-Rad, STAR72). Plates were then washed and TMB was
899 added. The reaction was stopped with sulfuric acid once the wells containing the lowest dilutions
900 of TMB began to develop visually and the absorbance of each well was determined. Complement
901 deposition is reported as an area under the curve.

902 **Single cell BCR sequencing**

903 CD4bs-specific GC B cells were FACS-sorted from inguinal lymph nodes harvested from VH1-2
904 mice immunized with protein or DNA-scaffolded immunogens, gated on $B220^{+}/CD38^{lo}GL7^{hi}/IgM^{-}$
905 $IgG^{+}/eOD^{++}KO^{-}$ populations. We generated BCR libraries from whole transcriptome amplification
906 (WTA) products produced using the Smart-Seq2 protocol on the FACS isolated B cells[89]. The
907 WTA products underwent two 0.8x (v/v) SPRI bead-based cleanups and were verified using High
908 Sensitivity D5000 ScreenTape (Agilent Technologies Inc) and quantified and normalized using the
909 Qubit dsDNA HS Assay kit (Thermo Fisher Scientific, cat # Q32854). To enrich the BCR
910 sequences (FR1 to CDR3), corresponding heavy and light chains were amplified (HotStarTaq
911 Plus Master Kit, Qiagen, cat #203645) with a pool of partially degenerate primers specific against
912 all possible IGHV (human) or IGLV (mouse) and IGKV (mouse) segments in the FR1 region (final
913 concentration: 10 μM each) and reverse primers against the heavy or light constant regions (final
914 concentration: 10 μM each)[89]. These primers were also built with attachments to the Illumina P7
915 (V region) and P5 (constant region) sequences[89]. The amplicons were quantified and normalized
916 following BCR amplification and SPRI cleanup, after which cellular barcodes and Illumina
917 sequencing adapters (Nextera XT Index Adapters, Illumina Inc.) were added to each amplified
918 heavy and light chain using step-out PCR (Kapa HiFi HotStart ReadyMix; Fisher Scientific cat #
919 50-196-5217). After another SPRI cleanup the HC and LC samples were pooled and the single-
920 cell BCR libraries were sequenced via paired-end 250x250 reads and 8x8 index reads on an
921 Illumina MiSeq System (MiSeq Reagent Kit v2 (500-cycle), cat# MS-102-2003). The BCR heavy
922 and light chains reads were then paired using the barcodes and the overlapping sequencing reads
923 were reconstructed with PandaSeq[90], and aligned against the human or mouse IMGT database[91].
924 Sequencing error correction was performed with MigMAP, a wrapper for IgBlast
925 (https://github.com/mikessh/migmap). Consensus V_H and V_L/V_K chain for each single cell was
926 achieved by collating all reads with the same CDR3 sequence and then calling the top heavy and
927 light chain sequences by frequency. The nucleotide sequences (full-length heavy chain
928 sequences) from the public BCRs bearing the short five amino acid CDRL3 were aligned with
929 unmutated germline (IGHV1-2*02) sequence using the ClustalW alignment tool in the MEGAx[92].
930 The phylogenetic trees were constructed using the neighbor-joining method with Poisson Model
931 in the MEGAx[93]. The reliability of the tree nodes was tested using the Felsenstein bootstrap
932 method with 500 replicates.

933 **Statistics**

934 Statistics were computed in GraphPad Prism v.9 as denoted in the figure captions. For flow
935 cytometry analyses, comparisons between two groups were made using a two-sided Student's t-
936 test or Mann Whitney U test if the sample size was too small to pass a normality test. For
937 experiments with comparison with 3 or more groups, we used one-way analysis of variance
938 (ANOVA) with host-hoc Tukey test for multiple comparisons. For data shown on log axes,

939 geometric means and geometric S.D. values are shown. No outliers were excluded. One mouse
940 from Fig.4 was excluded due to accidental pregnancy. Exact *P* values are denoted in the figures.
941 For all figures, NS is not significant ($P > 0.05$).

942 **Data and code availability**

943 All data generated or analyzed during this study are included in this article (and its supplementary
944 information files). Source data are provided with this paper. The raw imaging data are available
945 from the corresponding author upon request**.** BCR sequences identified in this study will be
946 deposited in GenBank prior to publication (accession numbers, TBD). No new code was
947 developed for this study.

948 **Methods References**

949 86. Shepherd, T.R., Du, R.R., Huang, H., Wamhoff, E.-C. & Bathe, M. Bioproduction of pure,
950 kilobase-scale single-stranded DNA. *Scientific Reports* **9**, 6121 (2019).
951 87. Williams, S. et al. in DNA Computing. (eds. A. Goel, F.C. Simmel & P. Sosík) 90-101
952 (Springer Berlin Heidelberg, Berlin, Heidelberg; 2009).
953 88. Scheres, S.H.W. RELION: Implementation of a Bayesian approach to cryo-EM structure
954 determination. *Journal of Structural Biology* **180**, 519-530 (2012).
955 89. Sangesland, M. et al. Germline-Encoded Affinity for Cognate Antigen Enables Vaccine
956 Amplification of a Human Broadly Neutralizing Response against Influenza Virus.
957 *Immunity* **51**, 735-749.e738 (2019).
958 90. Masella, A.P., Bartram, A.K., Truszkowski, J.M., Brown, D.G. & Neufeld, J.D. PANDAseq:
959 paired-end assembler for illumina sequences. *BMC bioinformatics* **13**, 31 (2012).
960 91. Shi, B. et al. Comparative analysis of human and mouse immunoglobulin variable heavy
961 regions from IMGT/LIGM-DB with IMGT/HighV-QUEST. *Theor Biol Med Model* **11**, 30
962 (2014).
963 92. Stecher, G., Tamura, K. & Kumar, S. Molecular Evolutionary Genetics Analysis (MEGA)
964 for macOS. *Mol Biol Evol* **37** (2020).
965 93. Kumar, S., Stecher, G., Li, M., Knyaz, C. & Tamura, K. MEGA X: Molecular Evolutionary
966 Genetics Analysis across Computing Platforms. *Mol Biol Evol* **6** (2018).

967

968 **Acknowledgements**

969 This work was supported by National Institute of Health grant R01-AI162307-03 (M.B., D.J.I.),
970 R01AI155447, P30AI060354, R01-AI153098 (D.L.), the Ragon Institute of Mass General Brigham,
971 MIT, and Harvard (D.J.I, D.L.), the Howard Hughes Medical Institute (D.J.I.), National Science
972 Foundation Fellowship 4000168384 (A.R.), and National Science Foundation Fellowship
973 4000189657 (G.A.K.), and Novo Nordisk Foundation NNF23OC0082848 (M.O.). This work was
974 supported in part by the Koch Institute Support (core) Grant P30-CA14051 from the National
975 Cancer Institute and by the National Institute of Environmental Health Sciences of the NIH under
976 award P30-ES002109.
977
978 We thank the Robert A. Swanson (1969) Biotechnology Center at the Koch Institute for technical
979 support, specifically the Flow Cytometry and Microscopy Facilities. We acknowledge MIT.nano for
980 the use of core characterization facilities and support from a core center grant, P30-ES002109.
981 We thank Xiao Wang for assistance in CryoEM grid preparation and imaging. We are grateful to

Benjamin Clancy for production of ssDNA scaffolds used in the study. We thank the Ragon Institute Flow Cytometry Core for assistance in FACS sorting. We are grateful to Fred Alt (source of V_H1-2 mice) and Boris Reizis (source of DNase I KO mice, originally from CMMR).

Author Contributions

A.R., G.A.K, M.B., and D.J.I conceived the study. A.R designed, folded, and characterized the nanoparticles in this study that have not previously described (d40_60mer, d30_30mer, d30_60mer). G.A.K. synthesized all DBCO-modified oligos used in this study. H.S. produced eOD immunogens in the study. T.S. provided lumazine synthase nanoparticles. M.O. performed transmission electron microscopy. A.R. and A.P.C. maintained all animal cohorts, and A.R. performed immunizations. A.R., A.P.C., M.O., V.R.L, and K.S. conducted animal procedures and tissue processing. A.R. conducted flow cytometry and microscopy experiments. J.C. and B.R. developed methods for DNase genotyping and provided support on DNase I KO experiments. L.R. and A.R. performed FACS sorting on antigen-specific B cells, and L.R. conducted whole transcriptome amplification, Illumina sequencing, and all subsequent analysis of BCR sequencing data. A.R., G.A.K., L.R., A.P.C., D.L., M.B., and D.J.I interpreted the results. A.R., M.B., and D.J.I. wrote the manuscript. All authors read and reviewed the manuscript.

Competing Interests

A.R., G.A.K., D.J.I., and M.B. are inventors on a patent application related to the DNA-VLP formulations described in this manuscript.

Supplementary Information is available for this paper.

Correspondence and requests for materials should be addressed to Darrell Irvine (djirvine@scripps.edu) and Mark Bathe (mark.bathe@mit.edu) .

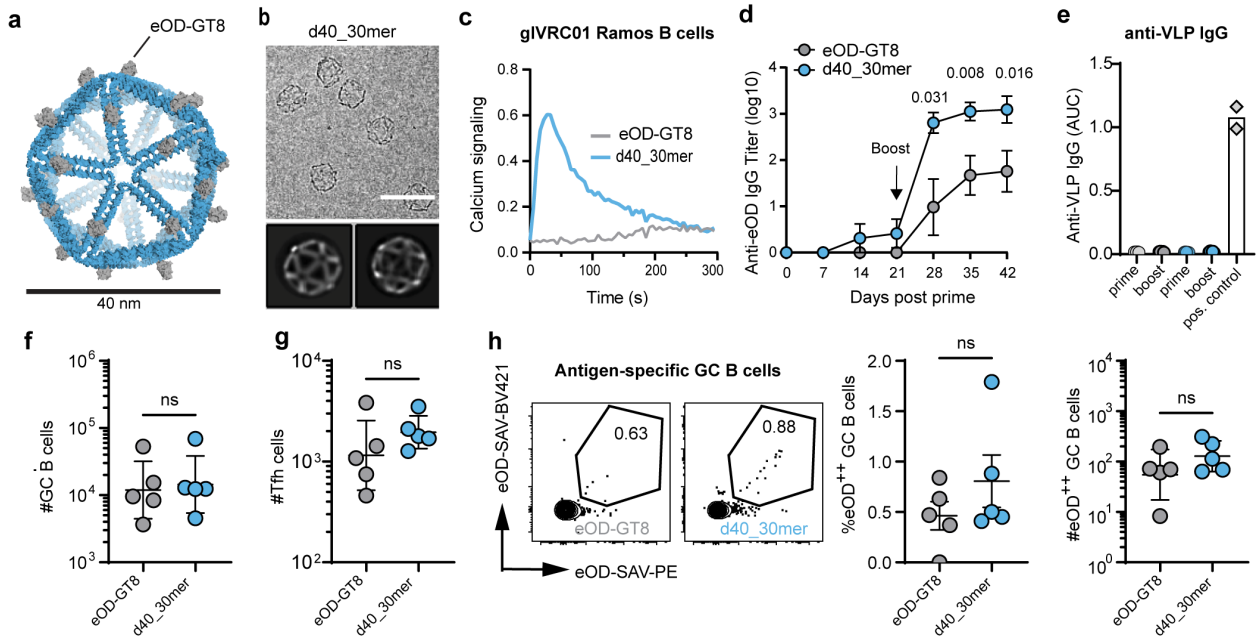

Fig 1. Nanoparticulate eOD-GT8 assembly on icosahedral DNA-VLP scaffolds. **a,** Atomic model of d40_30mer, which consists of an icosahedral DNA origami nanoparticle (52 base pairs/edge) with one eOD-GT8 antigen conjugated per edge of origami using SPAAC chemistry. **b,** Cryo-electron micrographs of d40_30mer and 2D class averages. The scale bar represents 50 nm. **c,** Representative calcium flux trace of glVRC01 B cells incubated with 5 nM eOD-GT8 monomer or d40_30mer from *n*=3 independent experiments. Traces were normalized to fluorescence background measured prior to antigen addition. **d,** C57BL/6 mice (*n*=5/group) were injected subcutaneously (s.c.) with equimolar doses of monomer or d40_30mer (equivalent to 5 µg of eOD-GT8 monomer) together with 5 µg SMNP adjuvant. Blood was collected weekly for serum eOD-GT8 antibody titer measurement by ELISA. Statistical significance was calculated using multiple Mann Whitney tests with Benjamini, Krieger, Yekutieli correction. **e,** Anti-origami IgG responses represented as area under the curve (log10) after prime (day 21) and boost (day 42) time points. An anti-dsDNA antibody was used as positive control. **f,** C57BL/6 mice (*n*=5/group) were primed with 5 µg of monomer or d40_30mer and sacrificed on day 14 for analysis of GC responses by flow cytometry. Total counts of GC B cells ($B220^{+}/CD38^{lo}GL7^{hi}$). **g,** Total counts of Tfh cells ($CD4^{+}/CXCR5^{hi}PD1^{hi}$). **h,** Representative flow plots showing eOD-tetramer staining, frequency of eOD^{++} GC B cells out of all GC B cells and counts of eOD^{++} GC B cells. Statistical testing was performed with Mann Whitney U tests.

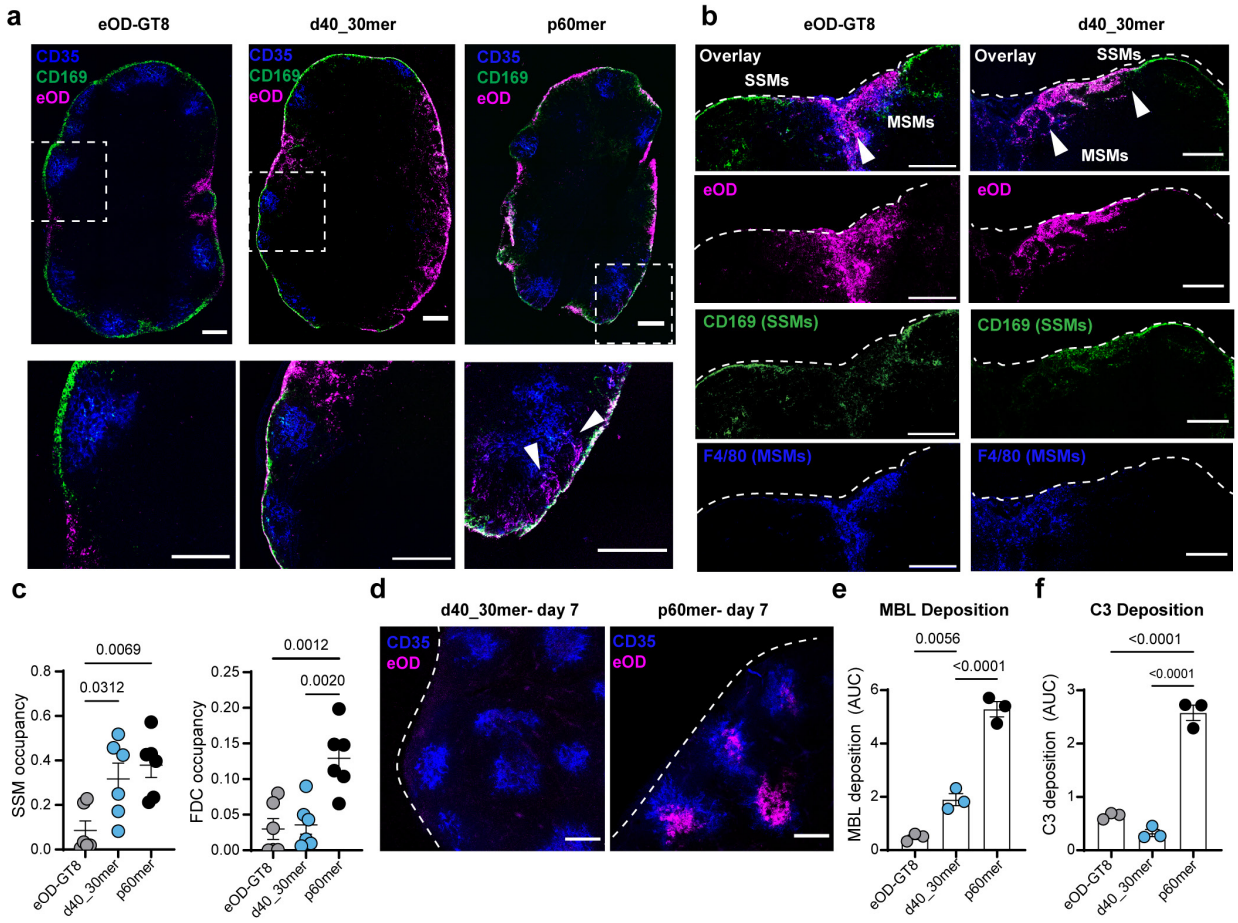

Fig. 2. d40_30mer DNA-VLPs are poorly retained on follicular dendritic cells in draining lymph nodes. **a,** C57BL/6 mice (*n*=3 mice, 6 lymph nodes/group) were primed s.c. with AF647-labeled eOD-GT8, d40_30mer, or p60mer. At 2 hr post-injection, inguinal lymph nodes were flash frozen, cryosectioned, and stained with anti-CD35 antibody (blue) and anti-CD169 antibody (green). Shown are representative lymph node images collected on a laser scanning confocal microscope, with close-up images of subcapsular sinus regions and follicles (lower panel). White arrows point to antigen (magenta) colocalized with FDC dendrites. Scale bars represent 200 µm. **b,** Lymph node sections from mice immunized with AF647-labeled eOD-GT8 monomer or d40_30mer (magenta) were stained with anti-CD169 (green) and anti-F4/80 (blue) antibodies for visualization of subcapsular sinus or medullary sinus macrophages, respectively. Arrows point to antigen colocalization with MSM or SSM populations. **c,** Quantification of fraction of $CD169^+$ SSMs and $CD35^+$ FDCs containing antigen at 2 hrs. **d,** Optically cleared inguinal LNs 7 days after immunization with AF647-labeled d40_30mer or p60mer. Follicles were labeled *in situ* by pre-injection of anti-CD35 antibody prior to fixing and clearing. Scale bar = 200 µm. **e,** MBL deposition measured by ELISA. Antigen formulations were immobilized on assay plates and treated with dilutions of fresh mouse serum. Anti-MBL antibody was used to detect MBL deposited on the antigens. **f,** C3 deposition measured by ELISA. Antigen formulations were immobilized on assay plates and treated with dilutions of fresh mouse serum. Anti-C3 antibody was used to detect C3 bound to the antigens. Statistics were calculated with one-way ANOVA with post-hoc Tukey test.

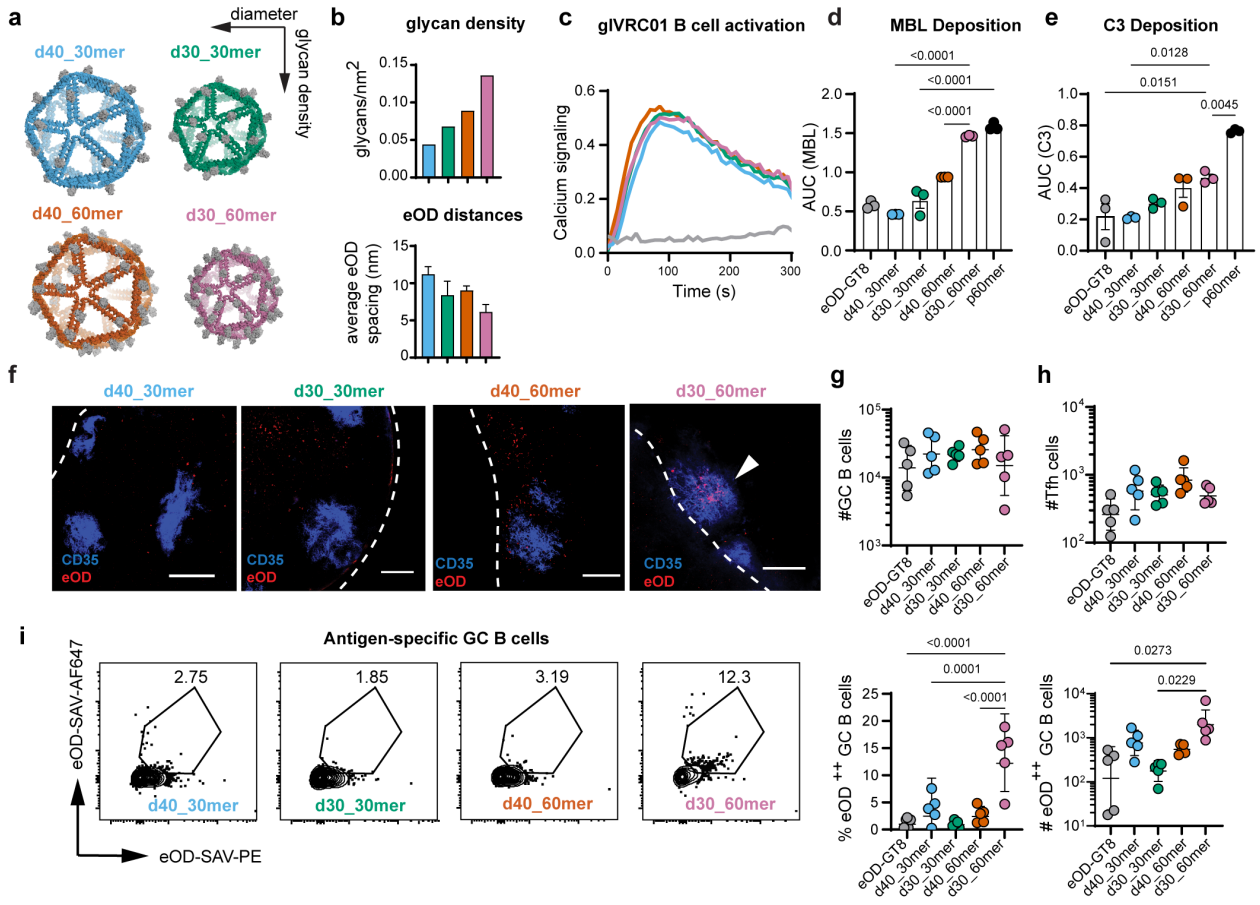

Fig. 3. High density antigen display enhances lectin pathway activation, FDC targeting, and antigen-specific GC B cell responses. a, Atomic models of icosahedral DNA origami nanoparticles with diameters of 30 or 40 nm (d30_ and d40_) and eOD-GT8 valency of 30 or 60. **b,** Predicted glycan densities assuming 4 glycan sites per eOD and inter-antigen distances calculated as the average distance to neighboring 5 antigens based on atomic models. **c,** Representative calcium signaling of glVRC01 B cells incubated with eOD formulations from 3 independent experiments. **d,** MBL deposition on different VLPs following incubation in fresh mouse serum detected by ELISA. Shown is the area under the curve of three technical replicates. **e,** C3 deposition on different VLP formulations, assayed by incubating in dilutions of fresh mouse serum and detected by ELISA. Shown is the area under the curve from three technical replicates. **f,** DNA-VLPs were formulated with AF647-labeled eOD-GT8. C57BL/6 mice (*n*=3, 6 lymph nodes/group) were immunized s.c. with 10 µg of antigen with SMNP adjuvant. Anti-CD35 antibody was injected prior to necropsy for in situ labeling of FDCs. Inguinal lymph nodes were collected at 96 hrs and cleared for whole tissue imaging. Shown are representative follicles (projection over 100 µm). Scale bar represents 200 µm. **g, (**C57BL/6 mice (*n*=5/group) were primed with equimolar antigen doses (equivalent to 5 µg eOD-GT8) with SMNP adjuvant. Inguinal LNs were analyzed on day 14. Shown are total counts of GC B cells (B220+ CD38 lo GL7 hi) and **h**, total counts of Tfh cells (CD4+/CXCR5+ PD1+). Absolute counts plots are shown with log axes; geometric mean and geometric S.D. are shown **i,** Representative flow plots of eOD-tetramer staining (left) and frequencies and counts of eOD^{++} GC B cells. Absolute counts plots are shown with log axes; geometric mean and geometric S.D. are shown Statistical significance was determined by 1-way ANOVA with post-hoc Tukey test.

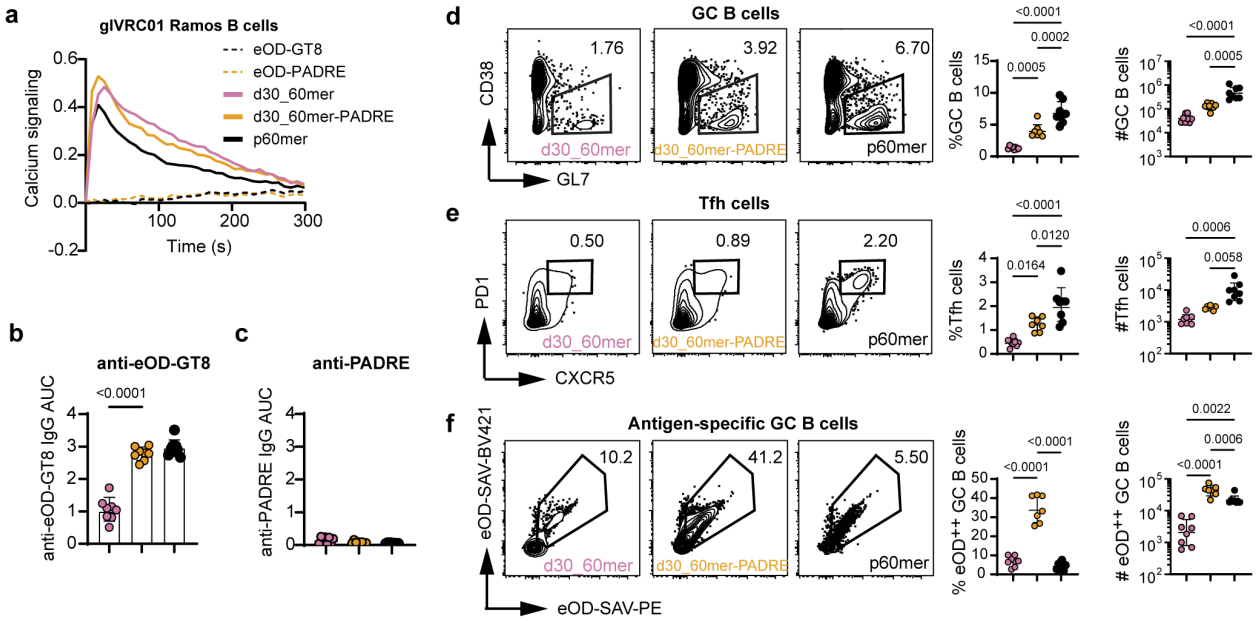

Fig. 4. Incorporating synthetic helper T cell epitopes boosts GC size after DNA-VLP vaccination. a, Representative calcium signaling traces from VRC01 Ramos B cells incubated with 5 nM eOD-GT8 equivalent concentrations of indicated particles (*n*=3 independent experiments). **b,** C57BL/6 mice (*n*=8 mice/group) were primed s.c. with equimolar doses (equivalent to 5 ug of eOD) of the 60mer formulations with SMNP and sacrificed on day 14 for serum titer analysis and germinal center analysis by flow cytometry. Anti-eOD-GT8 IgG titers were determined by ELISA (against eOD-GT8 without PADRE). Shown are AUC values (log10). **c,** Anti-PADRE IgG titers determined by ELISA against biotinylated PADRE peptide. Shown are AUC values (log10). **d,** Representative flow plots, frequencies (%GC out of total B cells), and counts of germinal center B cells (B220+/CD38lo GL7^{hi}). **e,** Representative flow plots, frequencies (%Tfh out of CD4 T cells), and counts of Tfh cells (CD4^{+} /CXCR5^{+} PD1^{+}). **f,** Representative flow plots, frequencies (%eOD^{++} out of GC B cells), and counts of antigen-specific eOD^{++} GC B cells. Absolute counts plots are shown with log axes; geometric mean and geometric S.D. are shown. Data was analyzed with one-way ANOVA with post-hoc Tukey test.

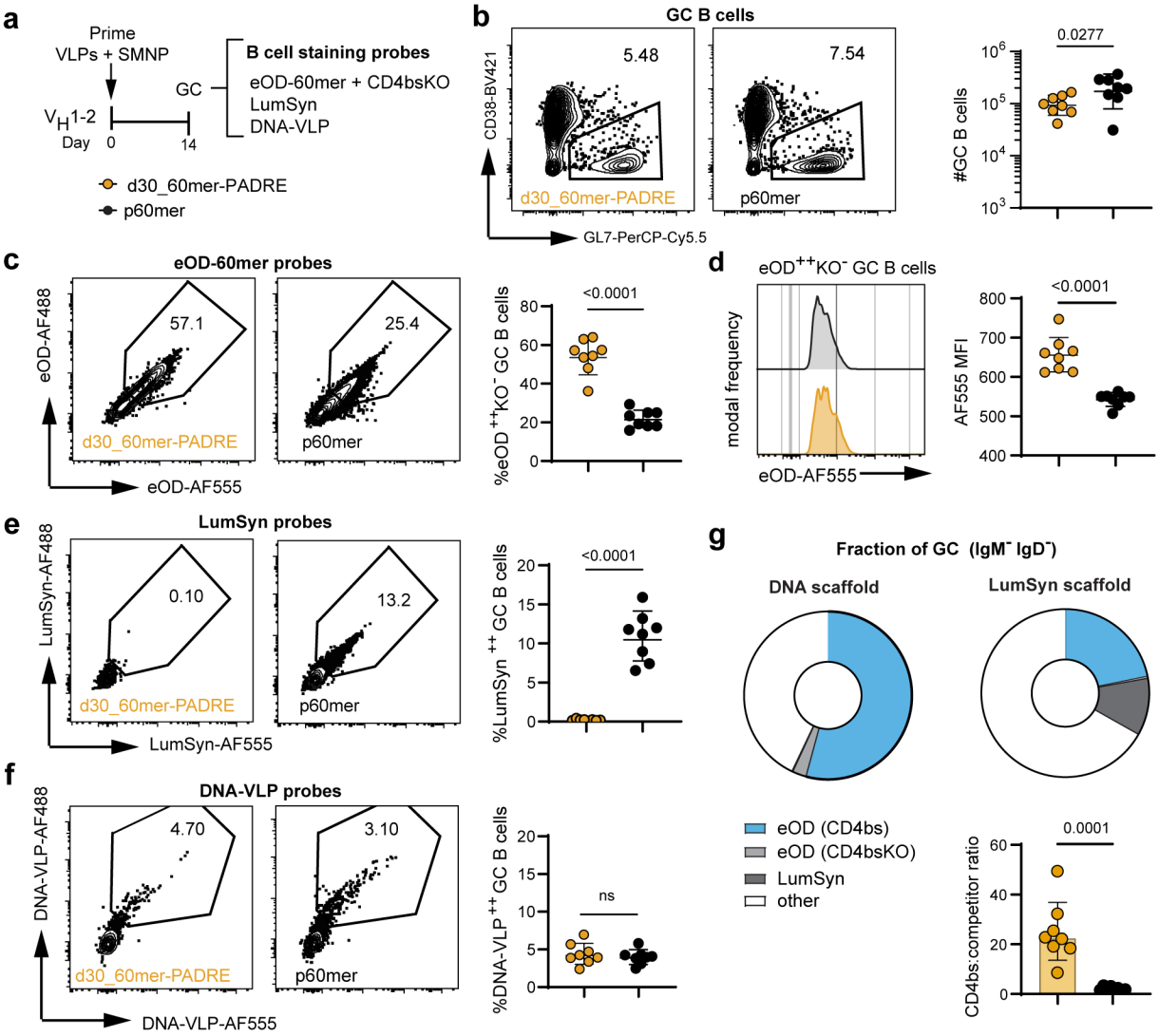

Fig. 5. DNA-VLPs produce focused germinal centers and prime VRC01-class precursors in humanized mice. a, Humanized V_H1-2 mice (*n*=8/group) were primed s.c. with 5 µg d30_60mer-PADRE or p60mer with SMNP, and inguinal lymph nodes were harvested on day 14. The lymphocytes were split into four samples and each stained with GC markers and fluorescently labeled antigen probes (eOD-60mer, bare lumazine synthase, or bare DNA-VLP (d30) probes). **b,** Total counts of B220^{+}/CD38^{lo}GL7^{hi} GC B cells. **c**, Representative eOD-60mer probe staining of GC B cells (left) and frequency of eOD-60mer^{++} cells out of IgM^{-} IgD^{-} GC B cells (right). **d,** Frequency of eOD-60mer^{++} eOD-CD4bs-KO^{-} (CD4bs+) out of IgM^{-} IgD^{-} GC B cells. **e,** Representative LumSyn staining of GC B cells (left) and frequency of LumSyn^{++} cells out of IgM^{-} IgD^{-} GC B cells (right). **f,** Representative DNA-VLP (d30) staining of GC B cells (left) and frequency of DNA-VLP^{++} cells out of IgM^{-}IgD^{-} GC B cells (right). Statistical significance was determined using one-way ANOVA with post-hoc Tukey test for b-f. **g**, Fraction of germinal center B cells that bound to each set of antigen or scaffold probes represented as parts-of-whole plot. The green slice represents on-target CD4bs-specific GC B cells. All other colors represent competitor B cells (eOD-CD4bs-KO or scaffold-specific B cells) or other cells not reactive with any probes.

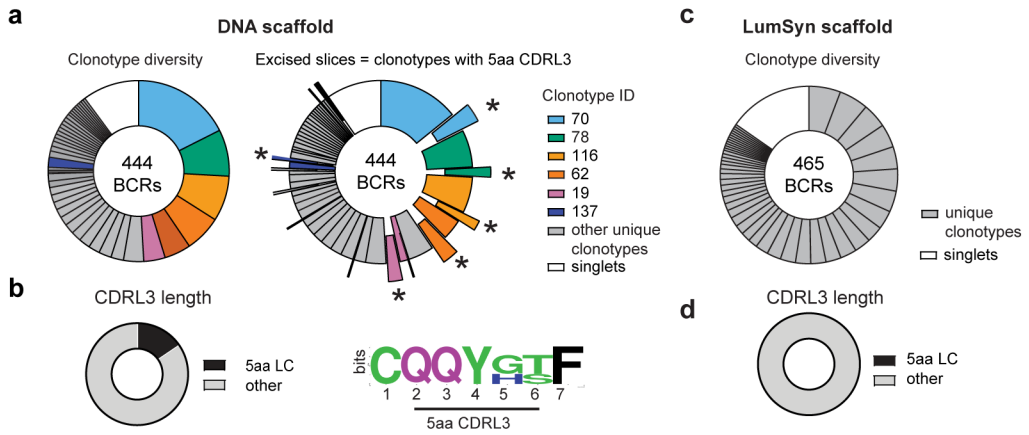

Fig 6. BCR sequencing reveals DNA-60mers effectively prime VRC01-class precursors in early GCs. **a,** BCR sequencing analysis of CD4bs-specific GC B cells (B220^{+} /GL7^{hi} CD38^{lo}/ IgM^{-} IgG^{+}/ eOD^{++} KO^{-}) isolated from V_H1-2 mice (*n*=2) immunized with d30_60mer-PADRE at day 14. (Right) B cell clonotypes were assigned based on shared CDRH3 usage. Shown in color are the top expanded clonotypes; the excised slices contain clonotypes with the short 5 amino acid CDRL3 marking the VRC01-class precursors. Asterisks represent shared public clones (shared VDJ/VJ origin) that contain the VRC01 class signature and were identically expanded in the different vaccine recipients. **b,** Distribution of light chain lengths in GC B cells from d30_60mer-PADRE immunization (right). Sequence conservation in light chains represented as a logo plot showing enrichment of VRC01-class motifs (left). **c,** Clonotype diversity in CD4bs-specific GC B cells from V_H1-2 mice (*n*=2) immunized with p60mer. **d,** Distribution of light chain lengths in GC B cells from p60mer immunization. No 5 amino acid CDRL3 light chains were expanded by the p60mer at this early timepoint.

Extended Data Figures

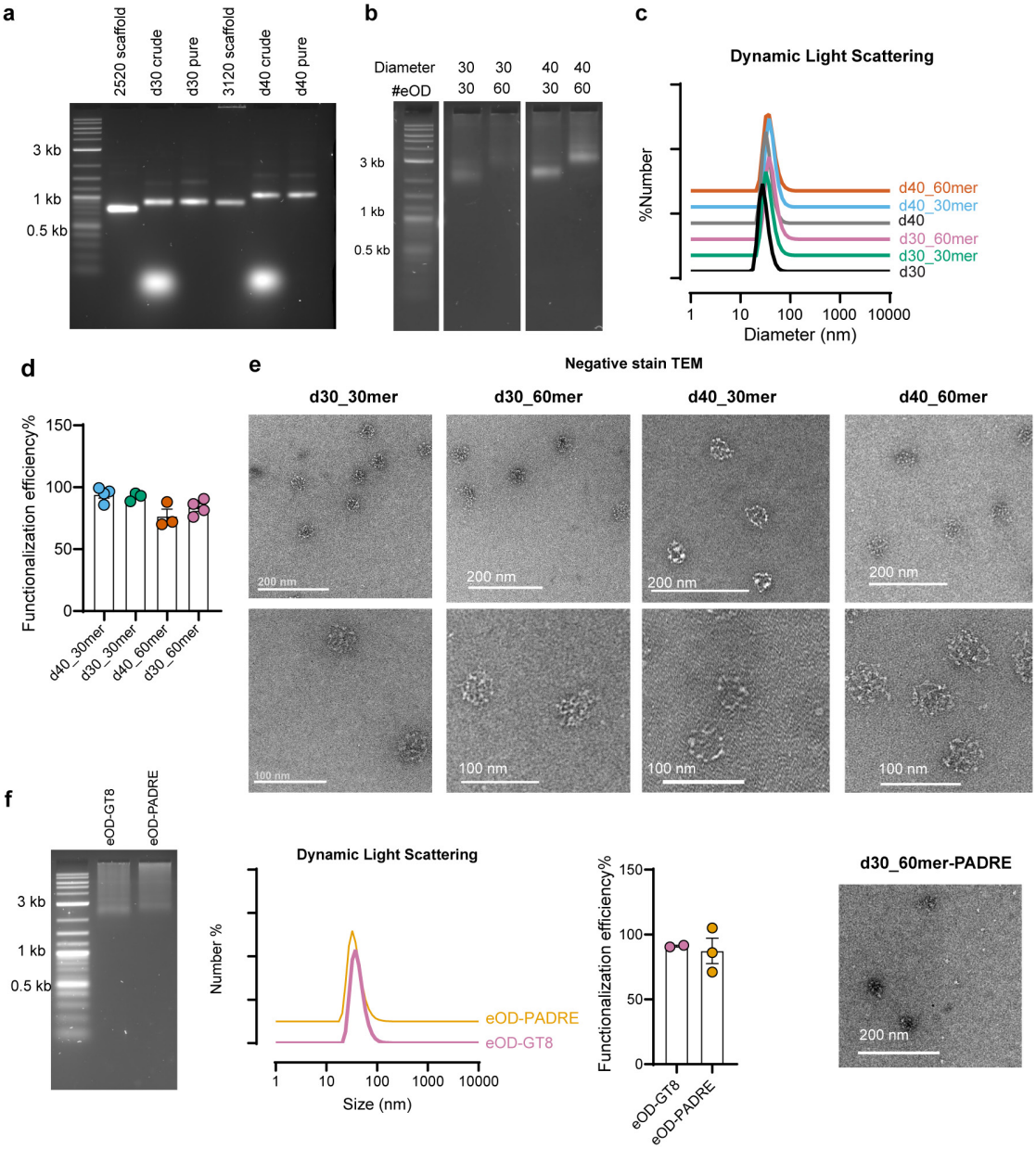

Extended Data Fig. 1. **Characterization of DNA-VLPs designed in this study. a,** Agarose gel electrophoresis (AGE) of ssDNA scaffolds, crude folded VLPs, and purified VLPs (after 3 rounds of Amicon filter centrifugation to remove excess staple oligos). Samples were run on a 1.6% agarose gel with SYBRSafe stain. **b,** AGE of DNA-VLPs following SPAAC reactions with eOD-Azide and purification with drop dialysis. **c,** Dynamic light scattering of DNA-VLPs pre- and post-antigen reaction. Shown are representative histograms, where x axis represents hydrodynamic diameter (nm) and y axis is the frequency by number. Each histogram trace is offset vertically for ease of visualization. **d,** Antigen functionalization efficiency from separate antigen preparations calculated from BCA assays. **e**, Negative stain transmission electron microscopy of each DNA-VLP design made in the study. Scale bars = 100 nm. **f**, Characterization of d30_60mer reacted with eOD-GT8 or eOD-PADE. Shown are representative AGE, dynamic light scattering, antigen functionalization efficiency, and negative stain TEM.

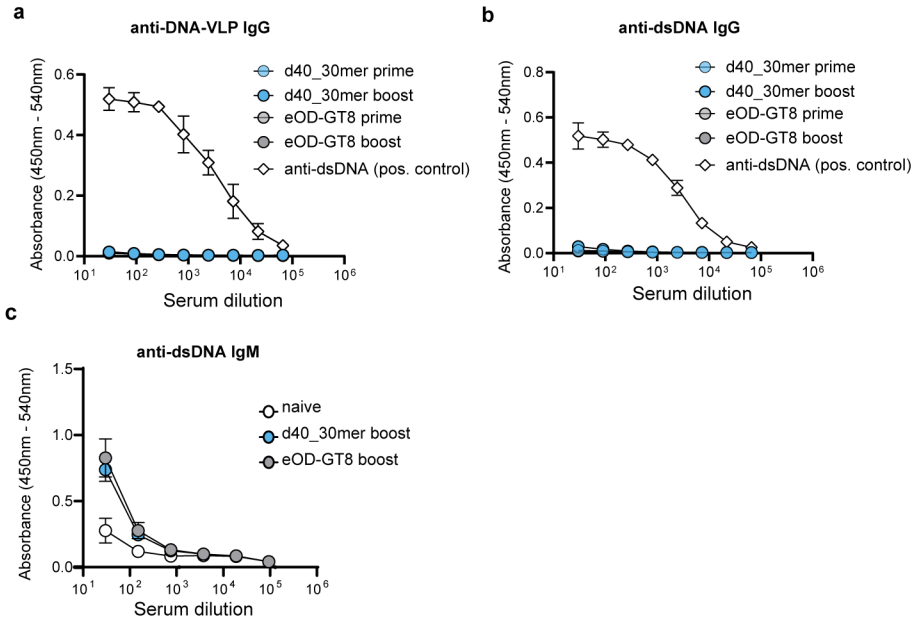

Extended Data Fig. 2. Analysis of anti-VLP and anti-dsDNA serum antibody responses, related to Figure 1. a, Raw serum dilutions curves of anti-origami ELISA shown in Fig 1H. Bare DNA-VLPs (d40) were used to coat ELISA plates, followed by incubations with serum from mice prime and/or boosted with eOD monomer or d40_30mer. Mouse anti-dsDNA IgG (Abcam 35I9) was used as a positive control. **b,** Anti-dsDNA ELISAs were measured by coating calf-thymus DNA on high binding ELISA plates and incubating with mouse serum samples from immunization studies. Shown are raw serum dilution curves (left) and area under the curve measurements (right). **c,** Anti-dsDNA IgM responses induced after vaccination with eOD-GT8 or d40_30mer. A commercial mouse anti-dsDNA ELISA kit was purchased from Alpha Diagnostics (cat# 5130) and used to assay IgM against dsDNA.

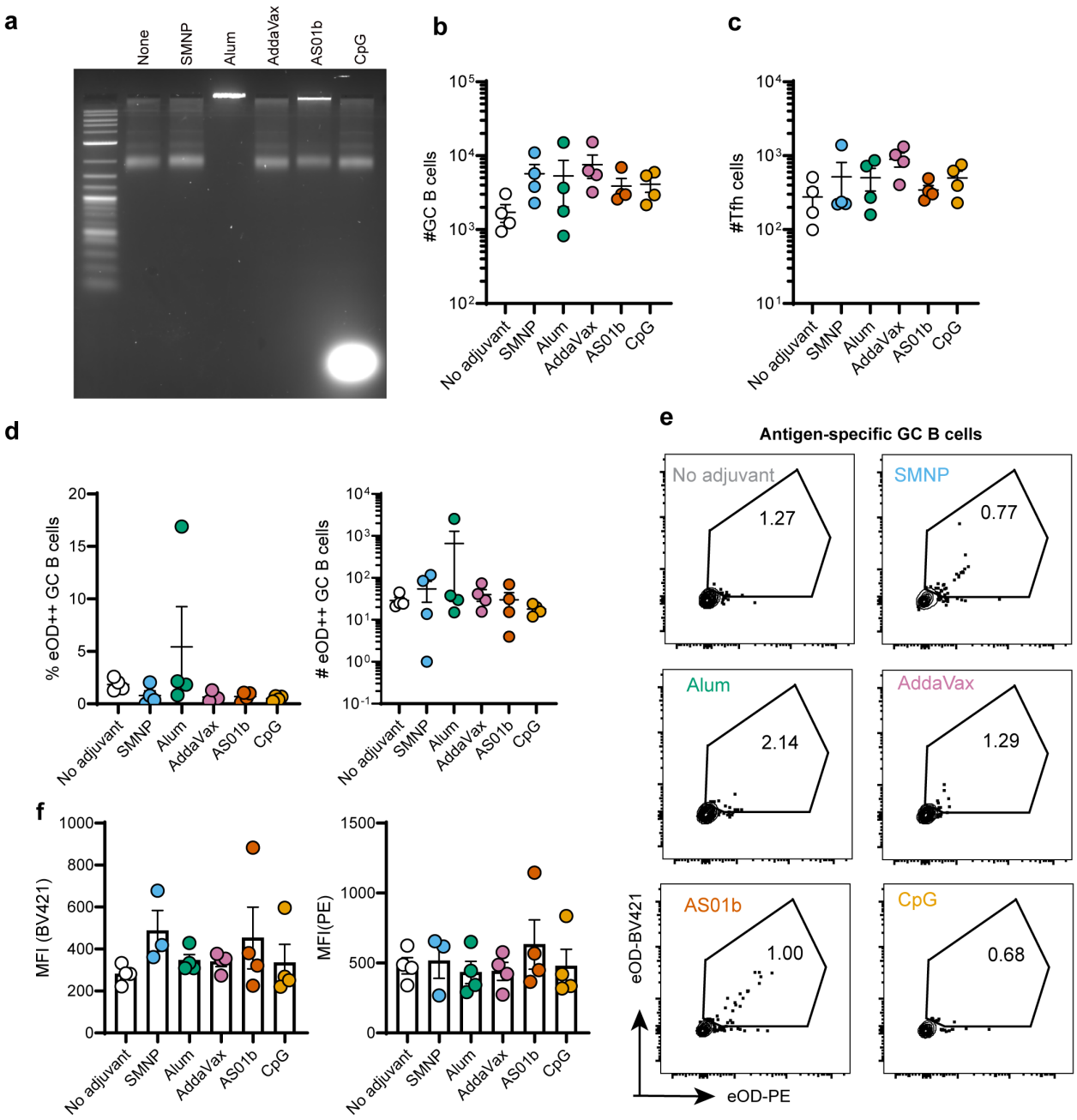

Extended Data Fig. 3. Comparison of GC responses induced by d40_30mer with common adjuvants. **a,** d40_30mer was formulated with different classes of adjuvants and gently mixed. Samples were loaded onto an agarose gel ten minutes after addition of adjuvant. Significant aggregation was observed for alum co-formulation and some minor aggregates are detected in the mixture with AS01b. **b,** Mice were primed with d40_30mer with different adjuvants and sacrificed at day 14. Inguinal lymph nodes were isolated and processed into a single cell suspension, then analyzed by flow cytometry. **c,** GC B cells (B220^{+} GL7 ^{hi}, CD38 ^{lo}), **d-g,** antigen-specific GC B cells, and follicular helper T cells (CD4^{+} CXCR5^{hi}, PD1^{hi}). No statistically significant difference was observed in cellular response between groups, as measured by one-way ELISA with post-hoc Tukey multiple comparison test. One mouse immunized with eOD-60mer (black) was used as validation for tetramer staining.

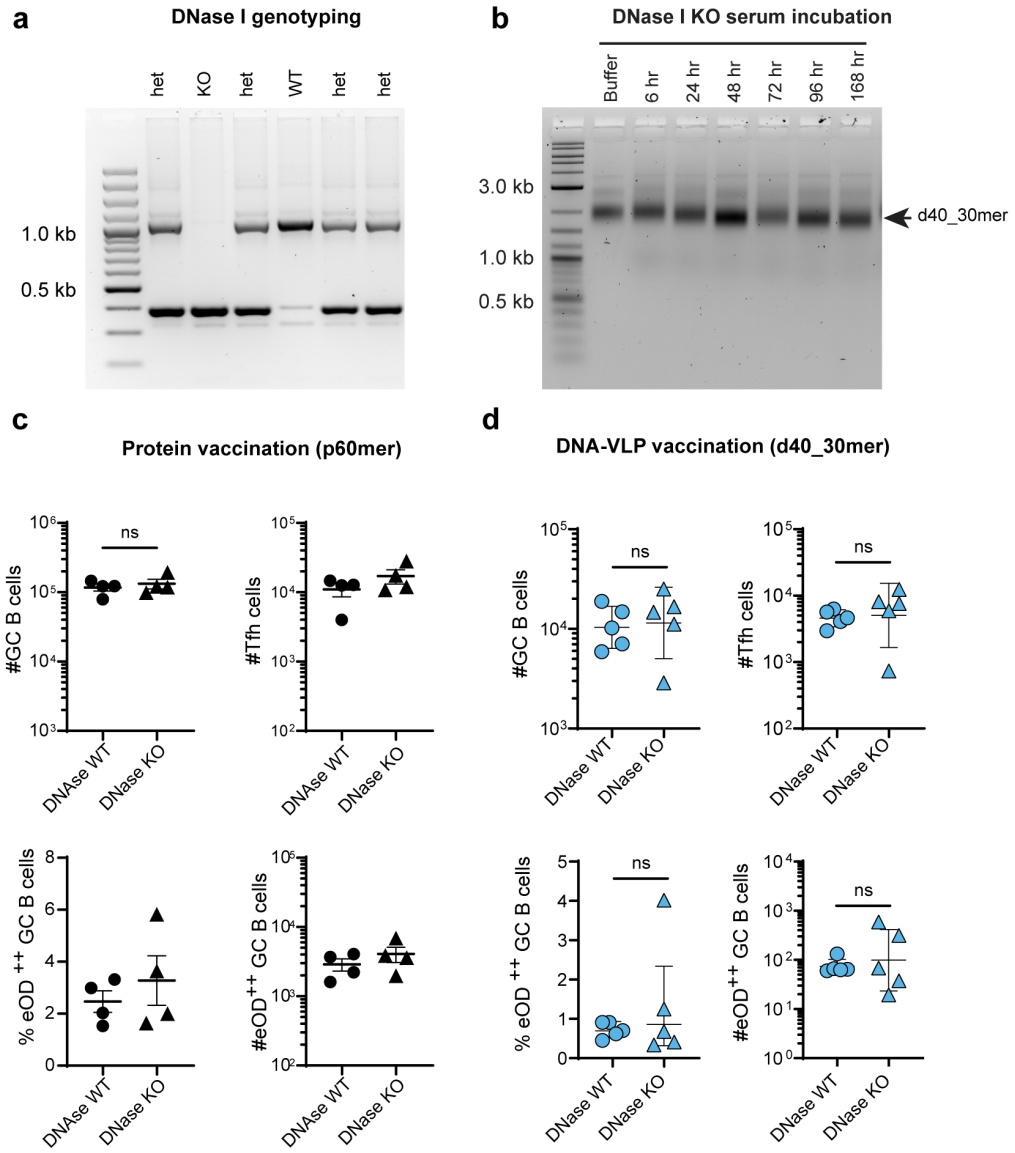

Extended Data Fig. 4. DNase I KO mice offer enhanced serum stability for DNA-VLPs but do not lead to enhanced GCs by d40_30mer vaccination. a, DNase I KO mice were genotyped using direct PCR from ear biopsies. Shown is a representative genotyping assay (homozygous KO with bands ~400 bp, WT with bands at ~1000bp, and heterozygous mice displaying both bands). **b,** Serum stability of d40_30mer incubated DNase I KO serum for up to 7 days (10% serum in PBS with calcium and magnesium). Shown are agarose gels with DNA-VLPs loaded at different time points. DNA bands do not degrade in the presence of DNase I KO serum. The slight shift downwards in the bands over time reflects the degradation of eOD-GT8 by serum proteases. **c**, WT or DNase I KO mice (n=4 mice/group) were immunized subcutaneously with 5 µg of p60mer with SMNP adjuvant. GC responses in inguinal lymph nodes were analyzed by flow cytometry on day 14. DNase I KO mice launch equally strong primary GCs in response to protein vaccination compared to WT mice. d, WT or DNase I KO mice (n=4 mice/group) were immunized subcutaneously with 5 µg of d40_30mer with SMNP adjuvant. GC responses in inguinal lymph nodes were analyzed by flow cytometry on day 14. D40_30mer primed similarly low responses in WT vs. DNase KO mice.

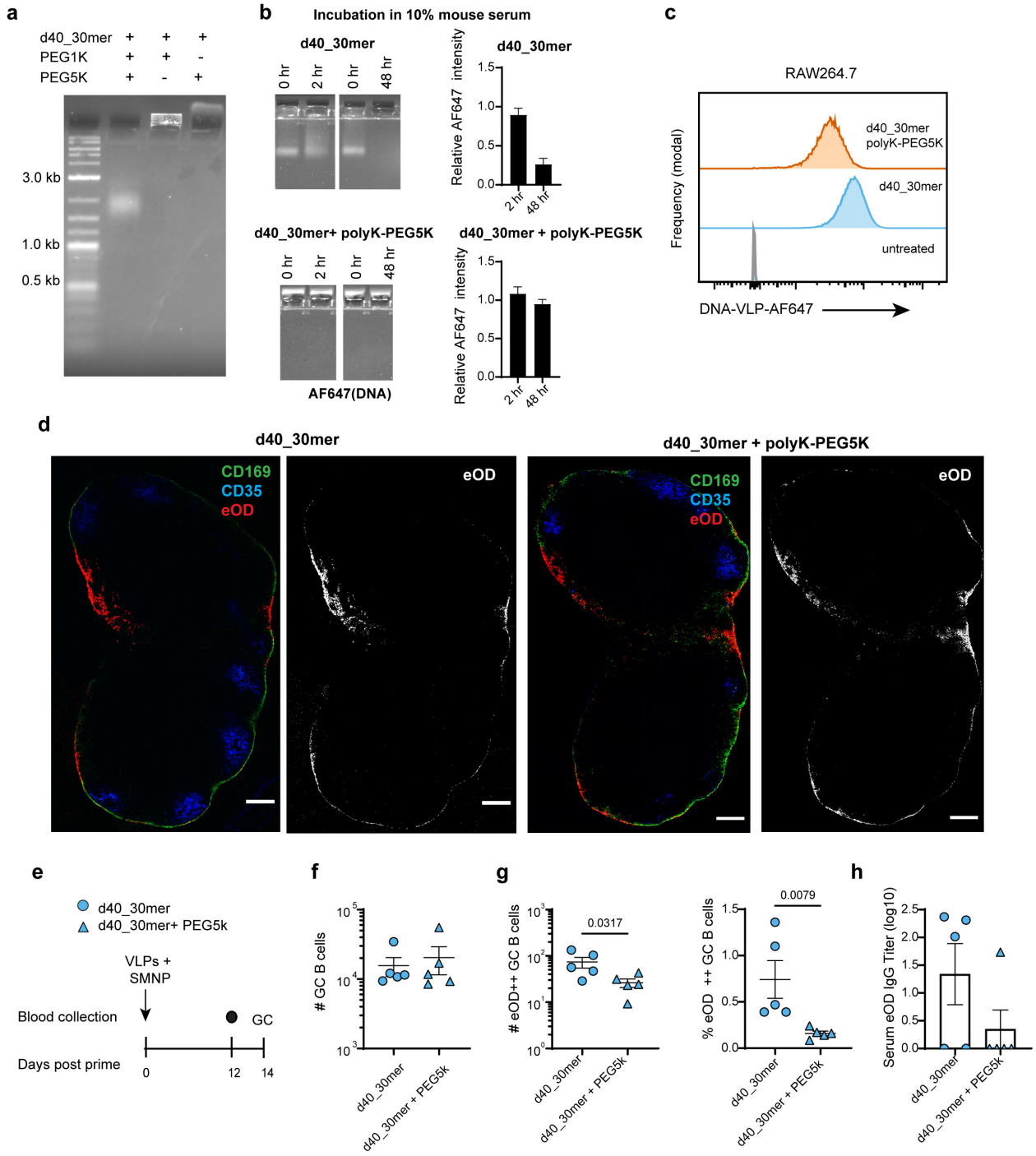

Extended Data Fig. 5. Polylysine-PEG coating on d40_30mer dampens GC responses. a, d40_30mer was coated with polylysine-PEG1K or 5K (Alamanda polymers) at 1:1 N:P ratio, as previously described by Ponnuswamy, et. al., and complexes were analyzed by AGE. Coated nanoparticles did not migrate through the gel due to neutralized charge. Significant aggregation was observed for the polylysine-PEG1K coating, so for subsequent studies only the PEG5K polymer was used. **b**, d40_30mer was formulated with 18x-AF647 dyes and 30 eOD-GT8 antigen and coated with polylysine-PEG5K. Bare and PEGylated VLPs were incubated with 10% fresh mouse serum (from naïve C57BL/6 mice) at 37°C for either 2 or 48 hours prior to analysis on AGE. Representative gels are shown (left) and relative AF647 band intensities (right) for bare

and PEGylated particles. **c,** AF647-labeled d40_30mer with or without polylysine-PEG5K were incubated with RAW264.7 macrophages for 1 hour and analyzed by flow cytometry. **d,** d40_30mer was formulated with AF647-labeled eOD-GT8 with and without polylysine-PEG5K and injected subcutaneously into C57BL/6 mice. Inguinal lymph nodes were flash frozen at 2 hours, cryosectioned, and stained with anti-CD35 (blue) and anti-CD169 (green). Representative nodes are shown (left- composite of three channels, right- greyscale image of nanoparticle distribution only). **e,** Immunization scheme for GC analysis. Mice were immunized with d40_30mer or d40_30mer coated with polylysine-PEG5k (5 µg eOD dose with 5 µg SMNP), and GCs were analyzed by flow cytometry at day 14**. f,** Total counts of GC B cells (B220+ GL7 hi CD38 lo). **g**, Total counts and frequency of antigen-specific GC B cells. Significance was determined by Mann Whitney U-test. **h**, anti-eOD IgG titer on day 14.

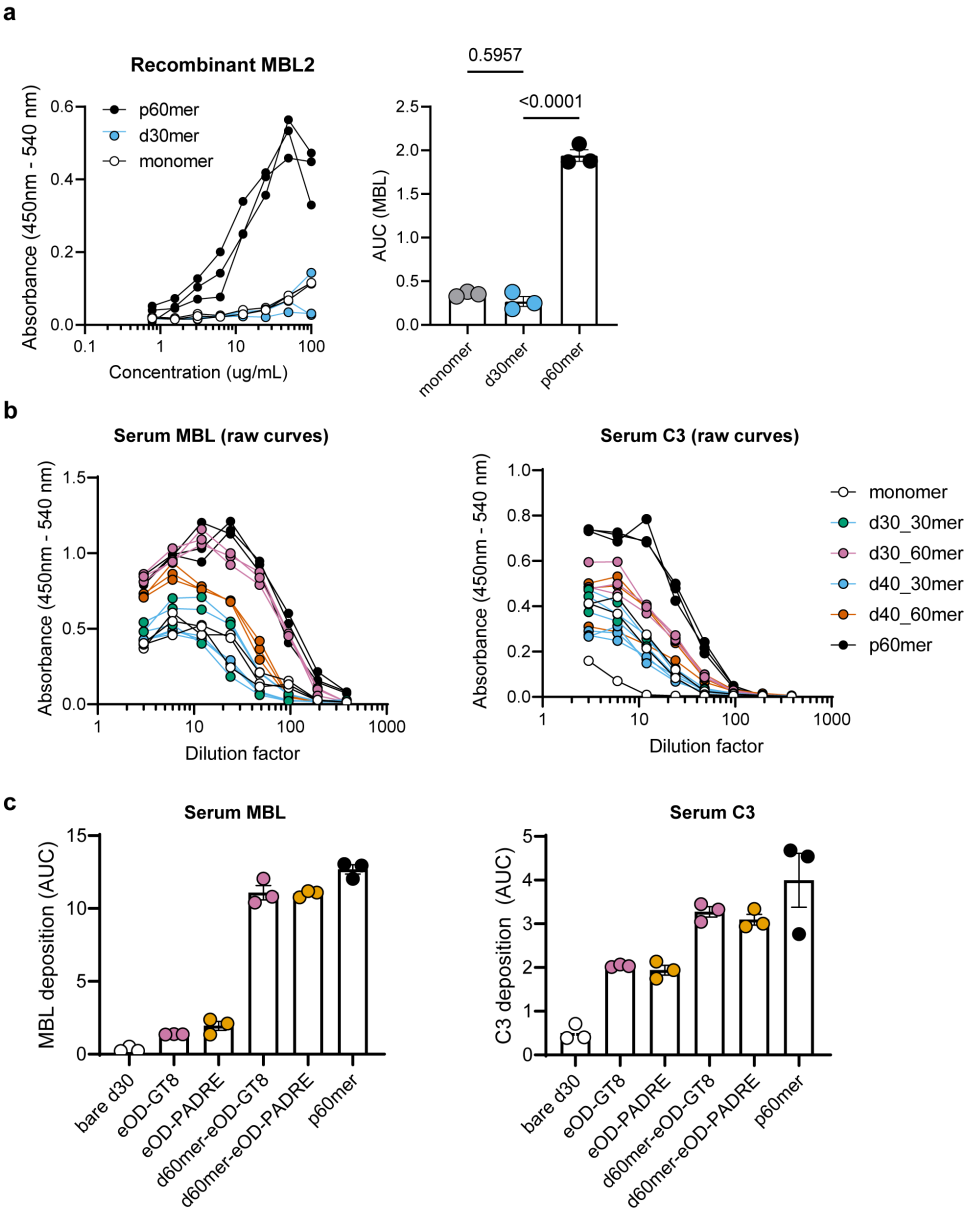

Extended Data Fig 6. Complement deposition on DNA-VLPs. (A) Binding of recombinant MBL2 to antigen formulations. Antigen formulations were immobilized on ELISA plates and incubated with dilutions of recombinant mouse MBL2 (R&D/Biotechne). MBL was detected using rat anti-mouse MBL2 (Abcam 14D12) and goat anti-rat HRP conjugate. Monomer and d40_30mer had minimal deposition of MBL2, while p60mer robustly bound MBL. Shown are raw dilution curves and A.U.C measurements. (B) Raw serum dilution curves for C3 and MBL ELISAs. Antigen formulations were immobilized on ELISA plates and incubated with dilutions of fresh mouse serum (each replicate is serum pooled from 3 mice). C3 was detected with rat anti-mouse C3 (Abcam 11H9) and goat anti-rat HRP secondary. MBL was detected using rat anti-mouse MBL2 (Abcam 14D12) and goat anti-rat HRP conjugate. Shown are raw dilution curves, and corresponding AUC measurements are shown in Figure 3 in the main text. (C) MBL (left) and C3 (right) deposition ELISAs using monomer or d30_60mers formulated with eOD-GT8 or eOD-PADRE. Shown are AUC measurements. P60mer is shown as an assay control.

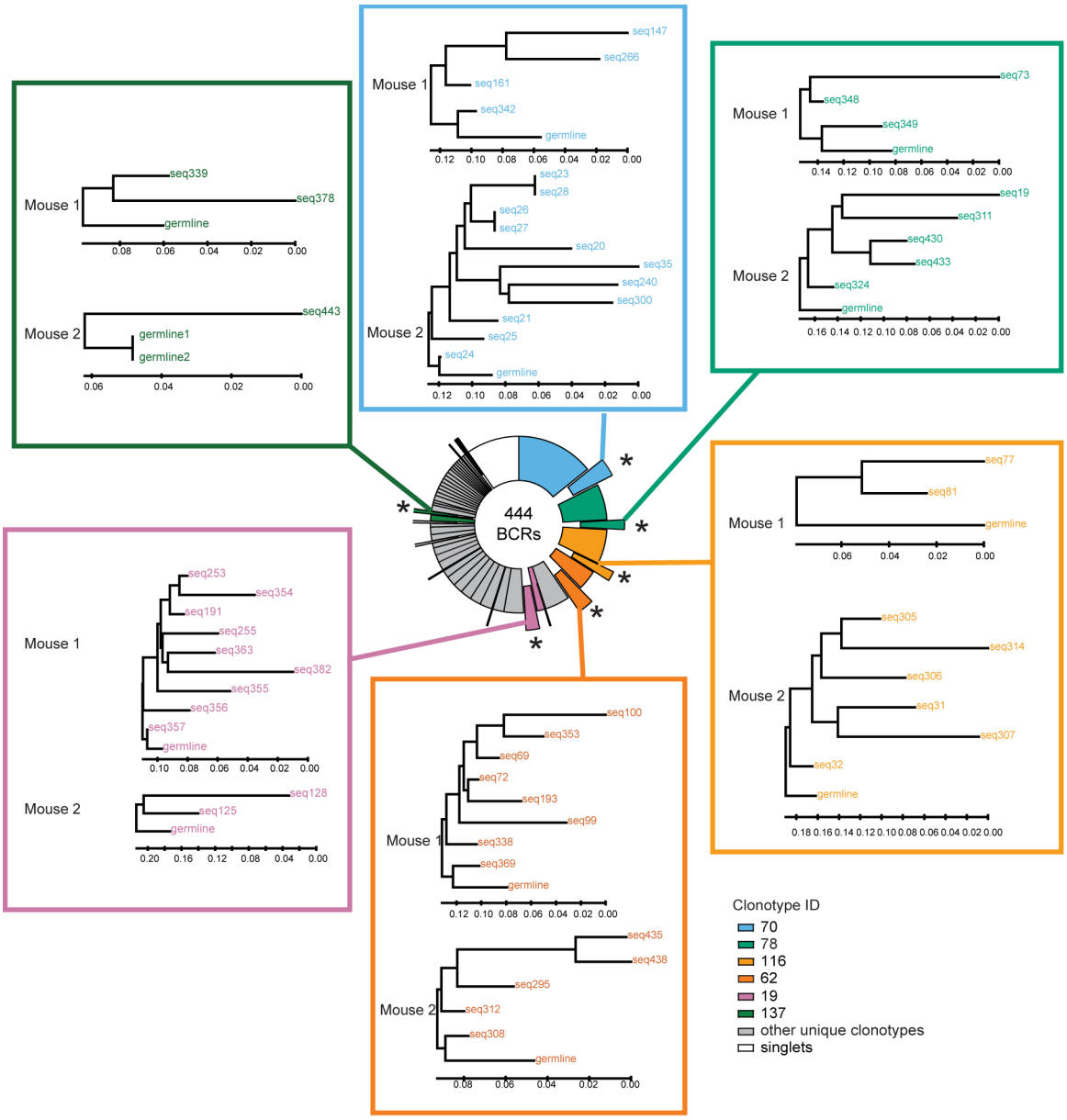

Extended Data Fig. 7. Reproducible expansion of public VRC01-class B cell clones by DNA-VLP. Phylogenetic trees of public B cell clonal lineages (shared VDJ/VJ origin within the different vaccine recipients) containing the 5 aa CDRL3 signature were constructed for each mouse. The unmutated IGHV1-2*02 nucleotide sequence was used as the reference sequence and the trees reflect mutational diversification of the HC. DNA-VLP expanded six public VRC01-class clones, presented here (Clone ID - 70, 78, 116, 62, 19 and 137). Bootstrap probability (>65%, 500 replicates) was used at the tree nodes to test reliability and the scale bar represents the nucleotide distance at an interval of 0.02 nucleotides per position in the sequence.

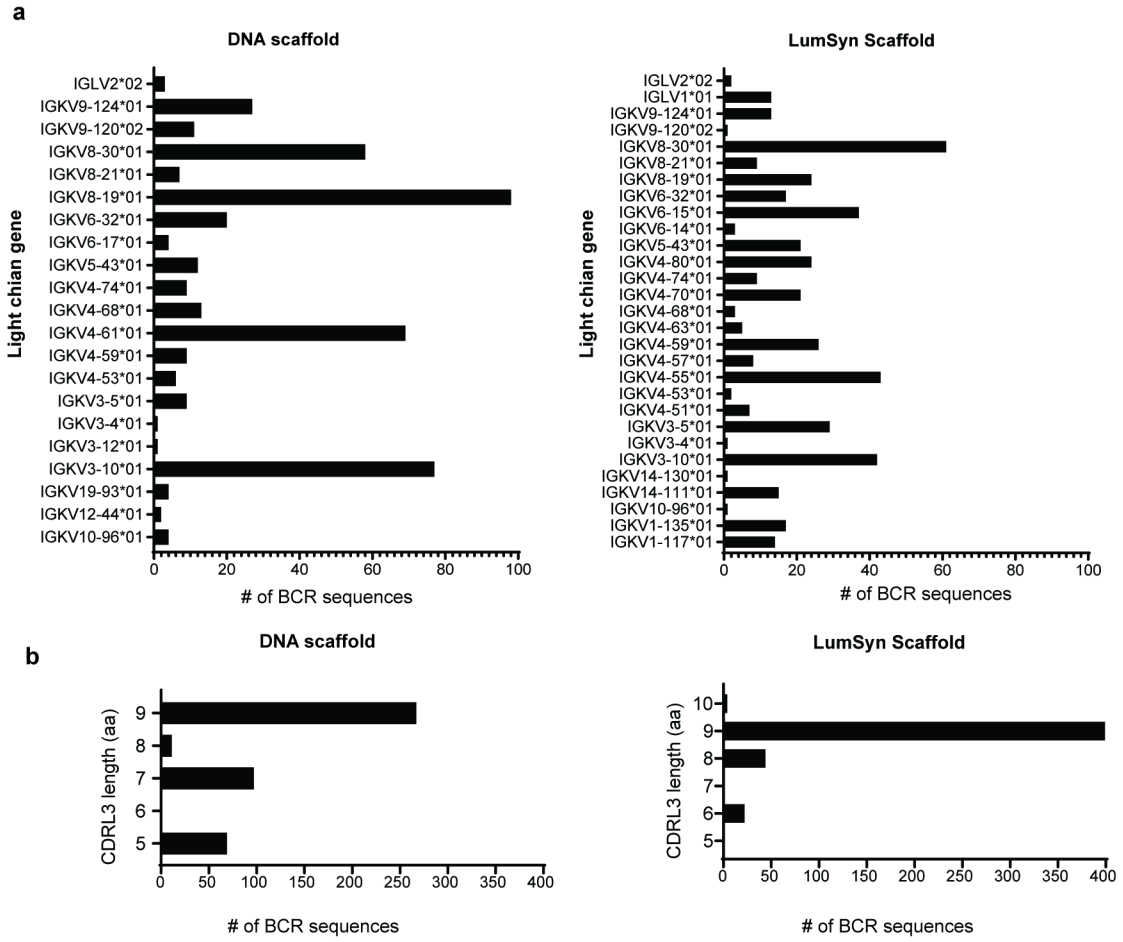

Extended Data Fig. 8. Mouse light chain gene usage and CDRL3 lengths within the eOD specific BCRs elicited by DNA-VLP or p60mer. **a,** Mouse IGKV or IGLV gene usage in the eOD specific BCRs expanded in the GC by each immunogen (n=444 BCRs for VLP-DNA; n=469 BCRs for p60mer, n=2 mice per immunogen). **b,** Corresponding CDRL3 lengths of these antigen specific BCRs. In the case of the 5 aa CDRL3 signature expanded by VLP-DNA, the LC gene used was exclusively IGKV4-61*01.

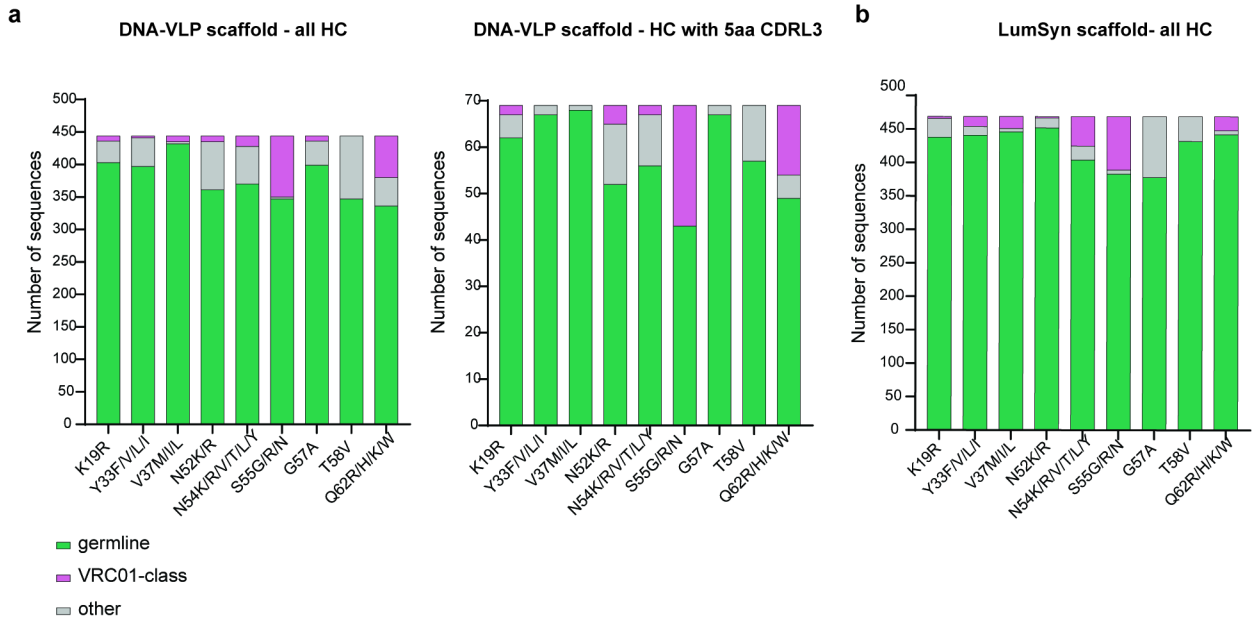

Extended Fig. 9. VRC01 mutations within the eOD-specific GC BCRs elicited by DNA-VLP or p60mer. a, stacked bar graph (left) denotes the quantity of VRC01-class mutations in the IGHV1-2*02 HC for all CD4bs-specific BCRs expanded by DNA-VLP (n=444 BCRs for VLP-DNA, n=2 mice). The adjacent graph (right) shows this for only BCRs bearing the 5 aa CDRL3 VRC01 signature. **b**, Stacked bar graph showing the quantity of VRC01-class mutations in CD4bs-specific BCRs expanded by p60mer n=469 BCRs, n=2 mice).